# Au nanoparticles decorated nanographene oxide-based platform: synthesis, functionalization and assessment of photothermal activity

*Fabio Vischio,[a,b] Livianna Carrieri,[c] Giuseppe Valerio Bianco,[d] Francesca Petronella,[e] Nicoletta Depalo,[b] Elisabetta Fanizza,[a,b] Maria Principia Scavo,[c] Luciano De Sio,[f] Antonella Calogero,[f] Marinella Striccoli,[b] Angela Agostiano,[a,b] Gianluigi Giannelli,[g] Maria Lucia Curri,[a,b,*] Chiara Ingrosso[b,*]*

*[a]Department of Chemistry, University of Bari, Via E. Orabona 4, 70125 Bari, Italy*

*[b]CNR-IPCF Bari Division, Via Orabona 4, 70125 Bari, Italy*

*[c]Personalized Medicine Laboratory, National Institute of Gastroenterology "S. De Bellis", Via Turi 21, 70013 - Castellana Grotte, Bari, Italy*

*[d]CNR-NANOTEC Bari Division, via Orabona 4, 70125 Bari, Italy*

*[e]CNR-IC, Via Salaria Km 29.300, 00015 Monterotondo, Rome, Italy*

*[f]Department of Medico-Surgical Sciences and Biotechnologies, Research Center for Biophotonics, Sapienza University of Rome, Corso della Repubblica 79, 04100 Latina, Italy*

[g]Scientific Direction, National Institute of Gastroenterology "S. De Bellis", Via Turi 27, 70013 Castellana Grotte, Bari, Italy

*E-mail: c.ingrosso@ba.ipcf.cnr.it, marialucia.curri@uniba.it, tel: +390805442027

ABSTRACT: A novel hybrid nanocomposite formed of carboxylated Nano Graphene Oxide (c-NGO), highly densely decorated by monodisperse citrate-coated Au nanoparticles (c-NGO/Au NPs), is synthesized and thoroughly characterized for photothermal applications. A systematic investigation of the role played by the synthetic parameters on the Au NPs decoration of the c-NGO platform is performed, comprehensively studying spectroscopic and morphological characteristics of the achieved nanostructures, thus elucidating their still not univocally explained synthesis mechanism.

Remarkably, the Au NPs coating density of the c-NGO sheets is much higher than state-of-the-art systems with analogous composition prepared with different approaches, along with a higher NPs size dispersion. A novel theoretical approach for estimating the average number of NPs per sheet, combining DLS and TEM results, is developed. The assessment of the c-NGO/Au NPs photothermal activity is performed under continuous wave (CW) laser irradiation, at 532 nm and 800 nm, before and after functionalization with PEG-SH. c-NGO/Au NPs composite behaves as efficient photothermal agent, with a light into heat conversion ability higher than that of the single components. The c-NGO/Au NPs compatibility for photothermal therapy is assessed by *in vitro* cell viability tests, which show no significant effects of c-NGO/Au NPs, as neat and PEGylated, on cell metabolic activity under the investigated conditions. These results demonstrate the great potential held by the prepared hybrid nanocomposite for photothermal conversion technologies, indicating it as particularly promising platform for photothermal ablation of cancer cells.

KEYWORDS: nanographene oxide, Au nanoparticles, hybrid nanocomposite, photothermal conversion, cytotoxicity tests, gastrointestinal cell lines

## 1. Introduction

Since its first isolation, graphene has been considered a carbon allotrope form of great interest due to its unprecedented properties promising for a plethora of applications [1].

Graphene Oxide (GO) is among the most interesting graphene derivatives as its oxygen-based functionalities enable its dispersion and processing from aqueous solutions, as well as plenty of possibilities for its further functionalization. GO aromatic domains make it an efficient photothermal material, able to absorb light from UV up to NIR region [2] and to turn photoexcitation into heat, properties that, combined with its superior thermal transport capability, have enhanced its relevance for photothermal technologies, as solar collectors, photothermal antibacterial surfaces, solar-driven water evaporation, photothermal catalysis and photothermal therapy [3] (PTT). Nanometer-sized GO, non-covalently coated by PEG and with an intense NIR absorption, has demonstrated a highly efficient tumour ablation in *in vivo* PTT treatment of mammary 4T1 cancer in mice [4].

Oxygenated functionalities of NGO basal plane can be used for its decoration with inorganic nanoparticles (NPs), by means of *in situ* and *ex situ* approaches. Au NPs immobilized onto NGO behave as photothermal sources through nonradiative decay undergoing strong plasmon interparticle coupling, [5] and also act as local nanoantennae [6] to enhance optical energy absorption of NGO at a selected plasmon frequency [7] by coupling with NGO surface plasmon polariton [8] and charge transfers [9], resulting in hybrid nanocomposites with enhanced photothermal conversion and efficiency [7,9]. Such nanocomposites, in addition, show a good degree of biocompatibility [10], which can be further improved coating GO with polyethylenimine (PEI) and polyethyleneglycol (PEG) for an effective internalization [11] in most cells, with low toxicity and without cell membrane damage [2], and for binding functional (bio)molecules [12]. *In vivo* PTT treatments of Ehrlich ascites tumour and ovarian SKOV-3 carcinoma in mice with PEGylated Au NPs decorated GO nanocomposites have been carried out, using NIR lasers, with an excellent performance ascribed to plasmonic coupling of Au NPs with GO [13].

Interesting multifunctionality and improved properties of these hybrid materials have prompted the advance of their synthesis routes; one of the most sustainable and facile comprises *in situ* reduction of tetrachloroauric acid ($HAuCl_4$), in presence of GO, by sodium citrate ($C_6H_5O_7Na_3$), acting, the latter, as reductant and, concomitantly, as stabilizing agent of the formed NPs. Such an approach does not require toxic and harsh reducing agents (i.e. hydrazine hydrate and sodium boron hydride), organic solvents and surfactants. Indeed, sodium citrate is a safe [14] and mild reducing agent, suited to synthesize aqueous dispersible Au NPs [15] for biomedical applications, as, due to its weak coordination to Au NP surface (6.7 kJ $mol^{-1}$) [16], it can be easily exchanged with a variety of biomolecules with different anchoring groups (i.e. thiolates, amines, carboxylates or phosphine). In addition, sodium citrate is preferred to more toxic organic surfactants (i.e. CTAB), that require, in fact, time-consuming purification or ligand replacing steps to produce colloidal NPs suspensions stable in biological media [17].

This approach relies on heteronucleation and growth of Au NPs onto GO oxygen functionalities, which behave as coordinating sites for such NPs, and, together, with carboxylic groups of sodium citrate, assist NPs formation controlling their morphology [18]. To the best of our knowledge, such an *in situ* synthesis approach has resulted, so far, only in polydisperse Au NPs and in a poorly dense GO sheets decoration [14,18,19]. A highly dense coating of monodisperse Au NPs is, instead, strongly amenable, as a higher number of photothermally active nanostructures significantly enhances light into heat conversion and increases surface adsorption sites for further biomolecules functionalization. Moreover, the role of the experimental parameters on the morphology of the resulting nanocomposites needs to be fully elucidated. Finally, a reliable quantification method of the Au NPs density onto the graphene sheets has been not yet established, while it would be relevant for rationalizing the preparation of the nanocomposites and their structure-properties relationship.

In this work, hybrid nanocomposites characterized by highly monodisperse NPs with a coating density enhanced with respect to similar state-of-the-art systems [14,18,19], have been synthesized in mild conditions, at a relatively low temperature (100°C), starting from tetrachloroauric acid trihydrate and trisodium citrate dihydrate, and NGO sheets, being the latter previously treated with NaOH and $ClCH_2COOH$ to increase -COOH groups density, by chemically converting native –OH, esters and epoxy groups into –COOH moieties by Williamson reaction [20].

The role of the synthetic parameters (i.e. temperature, reactant molar ratio, injection order and pH of c-NGO starting solution) has been investigated and a comprehensive systematic study of the spectroscopic and morphological properties of the prepared nanocomposites has been performed to get insight on the synthesis mechanism.

A new mathematical approach has been developed to define the amount of Au NPs per c-NGO sheet, by ingeniously merging experimental data obtained from Dynamic Light Scattering (DLS) and Transmission Electron Microscopy (TEM), computing sheets number from DLS measurements [21], avoiding overestimation due to c-NGO sheet overlapping in TEM micrographs [22].

Photothermal conversion efficiency of c-NGO/Au NPs nanocomposite has been evaluated, before and after PEGylation, under green (532 nm) and NIR (808 nm) continuous wave (CW) laser irradiation, at increasing power densities. Finally, the effect of the PEGylated hybrid nanoplatforms on cell viability has been investigated, *in vitro*, performing MTS assays on both normal epithelial cell line HCEC-1CT and metastatic gastric cancer cell line N-87. The results have shown that c-NGO/Au NPs exhibits good photothermal conversion properties, highlighting its relevance for photothermal technologies, and particularly for tumour ablation [23], also considering that they are not cytotoxic for normal and cancerous cells under the tested conditions.

## 2. Experimental section

*2.1 Materials.* Sodium hydroxide (NaOH), chloroacetic acid ($ClCH_2COOH$), hydrochloric acid (HCl), chloroauric acid trihydrate ($HAuCl_4 \times 3H_2O$, Au precursor) and trisodium citrate dihydrate ($C_6H_5O_7Na_3 \times 2H_2O$) were purchased from Sigma-Aldrich. Nano-Graphene oxide (NGO, 100 nm) was purchased from Graphene Supermarket. α-hydroxy-ω-mercapto poly(ethylene glycol) (HS-PEG, 2700 Da) was purchased from Iris Biotech GmbH. CellTiter 96 AQueous One Solution Cell Proliferation Assay (MTS) was purchased form Promega. All aqueous solutions were prepared using Milli-Q water (18.2 MΩ·cm organic carbon content $\geq 4$ μg $L^{-1}$) achieved by a Milli-Q gradient A-10 system.

*2.2 Preparation of carboxylated NGO (c-NGO).* 10 mg of NGO were dispersed in 5 mL of Milli-Q water and sonicated for 1 h in an ice cooled bath sonicator (Branson, 150 W) to exfoliate NGO.

Then, 1.2 g of NaOH and 1 g of $ClCH_2COOH$ were added, and the dispersion was sonicated for 3 h, for allowing, at first, conversion of epoxy into hydroxylate groups, and then into -COOH [24]. The as-synthesized suspension was stirred at 350 rpm for 15 h, and its resulting product was neutralized by HCl addition. Samples were purified by four cycles of ultracentrifugation and redispersion with ultrapure Milli-Q water (45000 rpm at 4°C for 20 min). Final pH of purified c-NGO dispersion in Milli-Q water was found ca. 6.83.

*2.3 Synthesis of c-NGO/Au NPs hybrid nanocomposite.* In a three-neck flask, 2, 1, 0.5 and 0.25 mL of a c-NGO dispersion (3.75 mg $mL^{-1}$) were added to 27 mL of ultrapure Milli-Q water at pH 6.83 and 11, by addition of NaOH, respectively, and such a dispersion was heated up to 30°C, 70°C or 100°C, under vigorous stirring. Once selected temperature was reached, 200 μL of Au precursor and 3 mL of citrate aqueous solutions were injected, and the reaction was allowed to proceed for 60 min.

Synthesis was performed by varying different experimental parameters including: i. injection order of Au precursor and citrate in the c-NGO starting aqueous dispersion, ii. citrate:Au precursor molar ratio as 80:1, 160:1 and 320:1, iii. c-NGO:Au precursor w/w as 0.25:1, 0.5:1, 1:1, 2:1 and 3:1 and iv. pH of the c-NGO starting dispersion.

The samples at the different citrate:Au precursor and c-NGO:Au precursor w/w ratio were obtained keeping fixed the amount of Au precursor and varying the amount of citrate and c-NGO, respectively. The as-synthesized samples were purified from the excess of citrate by multiple cycles of ultracentrifugation and redispersion in ultrapure Milli-Q water (45000 rpm at 4°C for 30 min).

*2.4 Functionalization of the hybrid nanocomposite with HS-PEG.* The nanocomposites synthesized with 0.25:1 and 0.5:1 c-NGO:Au precursor w/w ratio, selected because of their high NPs coating density, were surface functionalized with HS-PEG, by dispersion in aqueous solutions of HS-PEG, under mild stirring (150 rpm), at room temperature for 15 h. The HS-PEG functionalization was carried out with three distinct c-NGO:HS-PEG w/w ratio (1:1, 1:5 and 1:10) increasing the amount of HS-PEG and keeping fixed the amount of c-NGO.

The as prepared HS-PEG coated nanocomposites were purified from the excess of HS-PEG by dialysis against ultrapure Milli-Q water, using a 14000 Da cut-off dialysis tube stirred (150 rpm) at room temperature for 1 h.

### *2.5 Spectroscopy and morphological characterization.*

Raman spectroscopy was performed using the LabRAM HR Horiba-Jobin Yvon spectrometer with a 532 nm continuous excitation laser source. Measurements were carried out at a low laser power (1 mW) to avoid laser-induced damage of sample with an accuracy of 1 $cm^{-1}$. Spectrometer calibration was carried out using Raman signal collected from silicon substrate at 520 $cm^{-1}$.

Steady-state UV-Vis-NIR absorption spectroscopy measurements were performed by means of a UV−Vis−NIR Cary 5000 spectrophotometer (Agilent). All spectra have been registered in ultrapure Milli-Q water and normalized at the -C=C- characteristic absorption peak of NGO, the $\pi$-$\pi^*$ transition in the UV spectral region.

Mid-infrared spectra (4000 - 600 $cm^{-1}$) were recorded by a Varian 670 IR FTIR spectrometer equipped with a DTGS (Deuterated Triglycine Sulfate) detector. The spectral resolution was 4 $cm^{-1}$ and 64 scans were collected for each spectrum. For ATR measurements, a one-bounce 2 mm diameter diamond microprism was used as Internal Reflection Element (IRE). For the analysis, 5 μL of the sample dispersions were deposited by casting onto the upper face diamond crystal, then allowing solvent evaporation.

A Zetasizer Nano ZS, Malvern Instruments Ltd., Worcestershire, U.K. (DTS 5.00) was used to estimate the hydrodynamic size of the NGO and c-NGO sheets. Surface charge was determined by ζ-potential measurements carried out by laser Doppler velocimetry method, after sample dilution in ultrapure water. All data were reported as mean values ± standard deviation of three independent experiments.

Size and morphology of nanostructures were investigated by a Jeol JEM 1011 TEM operating at 100 kV, equipped with a W electron source and a high-resolution CCD camera. The sample deposition was carried out by dipping a 400-mesh carbon-coated copper grid in the aqueous sample dispersions, then letting the solvent to evaporate. Statistical analysis of Au NPs average size and size distribution was performed by using the freeware ImageJ analysis program.

### *2.6 In vitro* study in gastrointestinal cell lines.

*2.6.1 Cells cultures.* Normal Epithelial colon cell line (HCEC-1CT) and gastric carcinoma (derived from metastatic site) cell line (N-87) were purchased from ATCC. All the cell lines were cultivated according to retailer protocols [25]. Briefly, the normal colon cell line (HCEC-1CT) was cultured in 10% of Inactivated Fetal Bovine Serum (FBS) in COLO-Up medium, with sodium pyruvate, 4.5 g $L^{-1}$ glucose (GIBCO), 4 mM L-Glutamine (GIBCO) and 5 mL Pen-Strep (penicillin 10,000 u $mL^{-1}$, streptomycin 10,000 u $mL^{-1}$, Lonza Biowhittaker). The N-87 cells were cultured in RPMI medium, supplemented with 10% of FBS, sodium pyruvate, 4.5 g $L^{-1}$ glucose, 4 mM L-Glutamine and 5 mL Pen-Strep. Cells were grown until reaching semi-confluence, in a humidified incubator at 37°C with an atmosphere containing 5% of $CO_2$.

*2.6.2 Cell proliferation assay.* The HCEC-1CT and N-87 cells were seeded into 96-well plates at a density of $2 \times 10^3$ cells per well, following a protocol previously described [26]. Subsequently, the formulations, at concentration ranging from 35 to 60 μg $mL^{-1}$, were added to each well. The plates were incubated at 37°C for 72 h. Untreated cells were used as control. At the end of the treatment, 20 mL of the MTS reagent were added to the cells for 3 h at 37°C and the absorbance at 490 nm was measured by using a PerkinElmer Victor Plate Reader (Belgium). Statistical analysis was performed by means of one-way analysis of variance (ANOVA) by SIGMA-STAT 3.1 and T-test. When this analysis rejected the hypothesis of the mean equality among the groups, the Bonferroni methods was applied [27].

*2.6.3 Immunofluorescence for vimentin expression.* Both cell lines were seeded into 6-well plates at a density of $5 \times 10^4$ cells per well, at 37°C, following the protocols previously detailed [28]. Briefly the assay was performed to detect vimentin expression level in the cells treated with each formulation at all the investigated concentrations in the range from 35 to 60 μg $mL^{-1}$, as well as in the negative controls, respectively, after 72 h of treatment. Subsequently, the cells were washed with PBS, fixed with cold ethanol for 30 min at 4°C and permeabilized for 15 min with 0.5%

Triton X-100 in PBS. Then, the cells were blocked with 5% normal serum in PBS for 1 h at room temperature and incubated overnight at 4°C with the primary antibody against vimentin (1:400 rabbit polyclonal anti-vimentin from Cell signalling). The treated cells were then incubated with a specific green fluorescent conjugated secondary antibody (Alexa Fluor® 488 from Invitrogen) for 1 h and mounted by using prolong gold antifade reagent containing 4',6-diamidine-2-phenylindole dihydrochloride (DAPI, Vector). Images were acquired and analysed by using Eclipse Ti2 by Nikon fluorescence microscope. The images were acquired using a Kr-Ar laser and an Ar laser with 488 nm and 358 nm band-pass filters, respectively, for vimentin, green (488 nm) and for DAPI blue channel (358 nm), at 40X magnification. The fluorescence intensity of all the investigated samples was quantified at a fixed exposure, namely 300 ms time per acquisition.

## 2.7 Investigation of photothermal properties.

To study the photothermal properties of c-NGO, c-NGO/Au NPs and c-NGO/Au NPs-PEG a two-color thermo-optical setup was used. The thermo-optical setup uses continuous wave (CW) diode lasers (Coherent Powerline) operating at 532 nm and 808 nm.

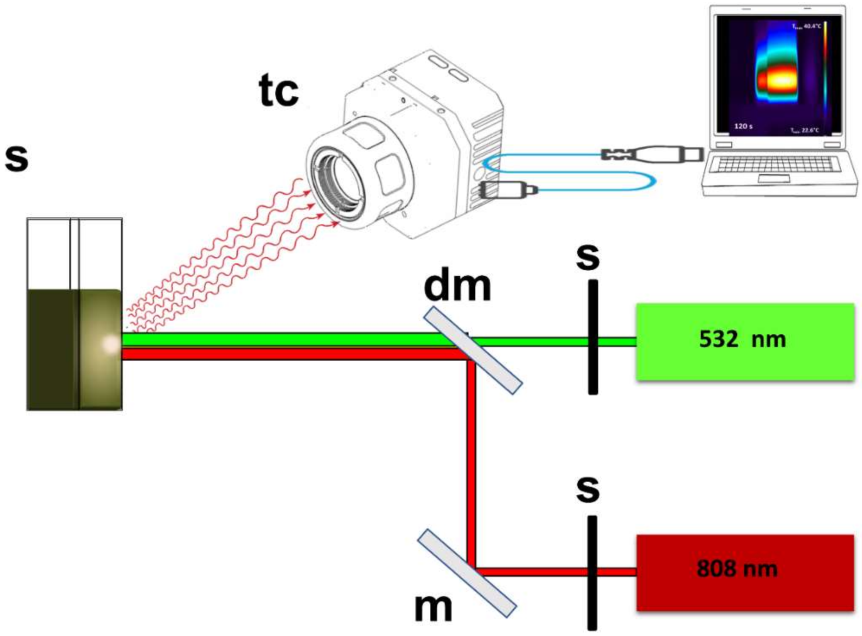

**Scheme 1.** Sketch of the dual color optical set-up used for the photothermal investigation. A quartz cuvette (s) filled with the samples (1 mL) is irradiated with two pump lasers beams emitting at 532 nm and 808 nm, respectively. The two laser beams are separately activated by the optical shutters (s) and subsequently are combined and co-launched using a mirror (m) and a dichroic mirror (dm). The spatial-temporal temperature profiles are detected with a high-resolution thermal camera (tc).

The green laser has a circular spot, while the near infrared laser beam has a rectangular profile that is converted into an almost circular spot using a 20 cm focal length elliptical lens. The photothermal measurements were performed in a quartz cuvette that was filled with 1 mL of the investigated colloidal dispersions at a concentration of 45 µg mL$^{-1}$. A high-resolution thermal camera (FLIR, A655sc) was used for mapping and identifying both the spatial heating distribution and the temperature profile under lateral pumping laser irradiation (Scheme 1).

The camera produces thermal images of 640 × 480 pixels with an accuracy of ±0.2 °C. It works seamlessly with proprietary software (FLIR ResearchIR Max) to record and process the acquired thermal data. Control experiments, for both lasers, were also performed on the c-NGO sample, at the maximum values of laser intensity.

## 3. Results and discussion.

### 3.1 Preparation and characterization of c-NGO.

Conversion of pristine hydroxyl, epoxy and ester groups of the NGO basal plane into –COOH [20] has been performed by the Williamson reaction, adding NaOH and $ClCH_2COOH$ to the NGO aqueous dispersions, to increase the density of -COOH groups. The TEM analysis shows that the resulting carboxylated NGO sheets (c-NGO) present almost electron transparent quadrangular-shaped 2D nanostructures, ca. 122.2 ± 31.0 nm in mean lateral size (Fig. 1A).

ATR-FTIR spectra of pristine NGO exhibit vibration modes of ethers, epoxy, carboxyl, hydroxyl and alkoxy groups (Fig. 1C). After treatment with NaOH and $ClCH_2COOH$, the spectra show: i. the increase of peak intensity of carboxylate ion asymmetric stretching ($\nu_{as\text{-}COO^-}$) at ca. 1586 cm$^{-1}$, with the corresponding symmetric stretching ($\nu_{s\text{-}COO^-}$) at ca. 1400 $cm^{-1}$ overlapped with the -OH bending ($\delta_{C\text{-}OH}$) expected in the same region, ii. the decrease of intensity of -C=O of carboxylic acid moieties at 1715 $cm^{-1}$, iii. the disappearance of the epoxy ring symmetric and asymmetric stretching ($\nu_{s\text{-}COC\text{-}}$, $\nu_{as\text{-}COC\text{-}}$) signal at ca. 1220 $cm^{-1}$ and 860 $cm^{-1}$, respectively, iv. the disappearance of asymmetric stretching of ether groups ($\nu_{as\text{-}COC\text{-}}$) at ca. 1240 $cm^{-1}$, v. the appearance of a medium signal at ca. 1250 $cm^{-1}$ and a weak band at 1080 $cm^{-1}$, both accountable to the asymmetric stretching of ether groups ($\nu_{as\text{-}COC\text{-}}$), and vi. the disappearance of the alkoxy groups stretching ($\nu_{s\text{-}COC\text{-}\ alkoxy}$) at 1050 $cm^{-1}$. These evidences can be reasonably explained on the basis of the Williamson reaction mechanism [20], that turns in grafting, onto the NGO basal plane, -$COCH_2COOH$ moieties.

Raman spectrum of pristine NGO shows two intense D and G+D' peaks at ca. 1340 $cm^{-1}$ and 1600 $cm^{-1}$, respectively (Fig. 1B), accounted for by collective in-plane -C-C- stretching modes of its aromatic rings[38] and $Csp_2$-$Csp_2$ stretching, respectively [29]. In the high wavenumbers region (Fig. 1C), the spectrum presents a large band, where the 2D, D+D' and 2D' peaks at ca. 2700, 2950 and 3200 $cm^{-1}$, respectively, can be distinguished. The feature at ca. 1600 $cm^{-1}$ can be ascribed to the superposition of the G and D' peaks, with the intensity of the D' signal, at ca. 1610 $cm^{-1}$, increasing with basal plane defectivity [30]. After treatment with NaOH and $ClCH_2COOH$, no changes, either in position of such a peak or in D/G+D' intensity ratio, are observed, thus confirming that no structural changes take place in NGO.

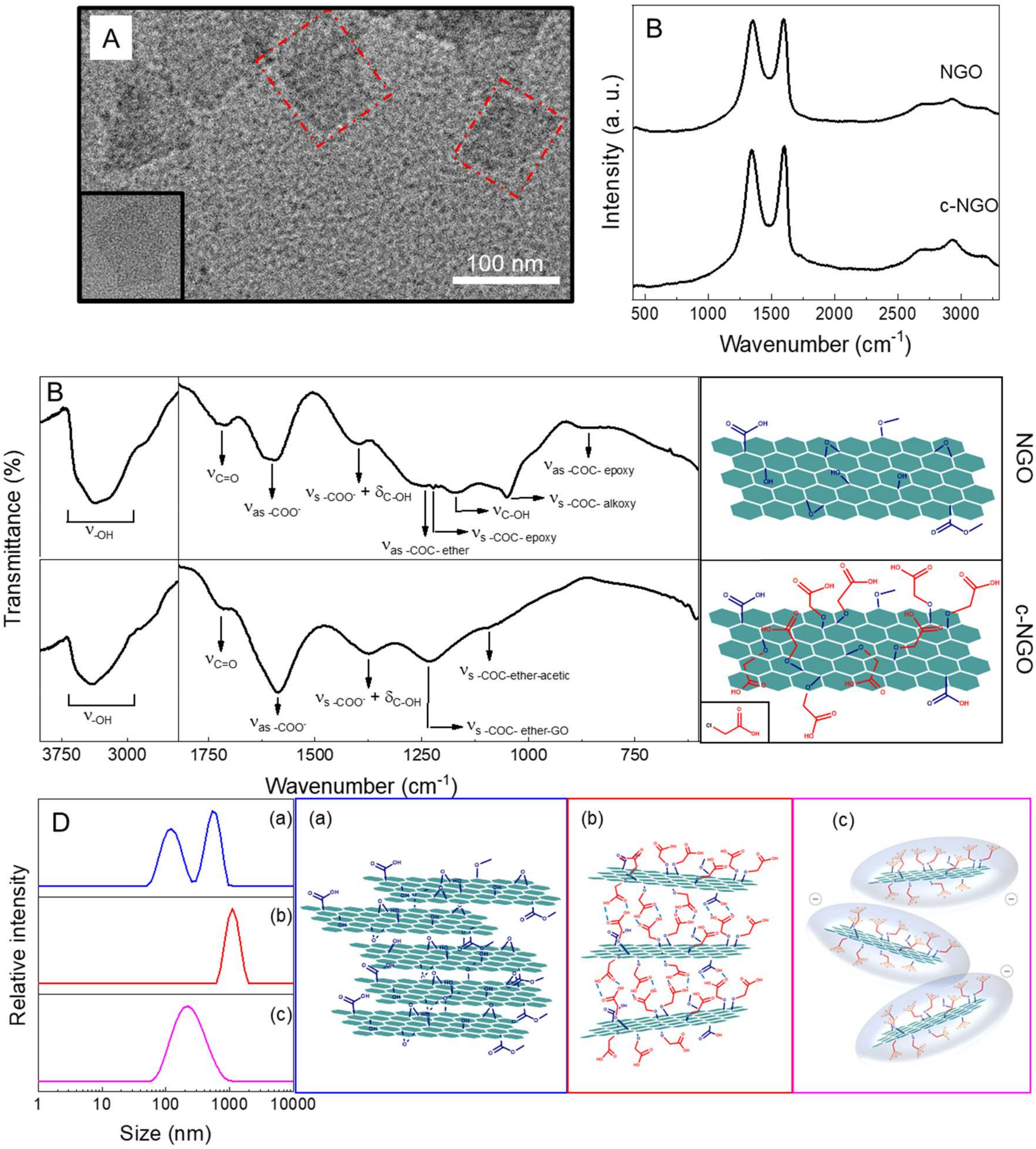

**Fig. 1.** (A) TEM overview of c-NGO from water (7.5 mg $mL^{-1}$) and (in the inset) from ethanol (3.5 mg $mL^{-1}$) dispersions. (B) Raman and (C) ATR-FTIR spectra with sketches of NGO and c-NGO. (D) DLS spectra and sketches of (a) NGO and (b) c-NGO in Milli-Q water at pH 6.83 and in (c) NaOH solution at pH 11. (The sketches are not drawn to scale).

An indicative estimation of the NGO sheets apparent size [21,31] has been provided by performing DLS measurements, that show for pristine NGO a bimodal size distribution with a peak at 128±1 nm (Fig. 1D (a)), in agreement with the size of a single sheet from TEM analysis (Fig. 1A), and another peak, at 520±2 nm (PDI=0.762±0.016), likely due to π-π stacked NGO sheets. The DLS spectrum of c-NGO (Fig. 1D (b)) presents, instead, a single population at 1198±22 nm (PDI=0.564±0.088), reasonably explained by aggregation phenomena due to intermolecular H-bonds among c-NGO sheets, that now feature the partially ionized -COOH groups at pH 6.83 in Milli-Q water. Such an explanation is confirmed by the disappearance of the population at 1198 nm upon addition of NaOH, that, increasing pH from 6.83 up to 11, leads to the complete–COOH ionization. Concomitantly, a monomodal population at 220 nm, reasonably ascribable to few-layered c-NGO sheets, appears (Fig. 1D (c)).

The ζ-potential value of untreated NGO sheets dispersed in Milli-Q water is ca. -34.7±0.8 mV, due to the presence of pristine carboxyl groups [31], and it decreases down to -40.1±1.1 mV, upon addition of NaOH at pH 11, thus confirming the increase of the amount of $–COO^-$ groups, that enhance the electrostatic repulsions among the c-NGO sheets, and, hence, their colloidal stability in aqueous solutions.

### 3.2 Synthesis of the c-NGO/Au NPs hybrid nanocomposite.

Au NPs have been heteronucleated and grown starting from the Au precursor, onto the oxygen functionalities of the c-NGO [18]. A systematic investigation of the effect of the c-NGO, Au precursor and sodium citrate·relative concentrations, reaction temperature, order of reactant injection in the reaction vessel and pH of the c-NGO starting dispersion, on the obtained nanocomposite spectroscopic and morphological properties, has been carried out, to get essential insights on the reaction mechanism, and thus, to control Au NPs size, size distribution, morphology, and NPs coating density onto the c-NGO (Scheme 2).

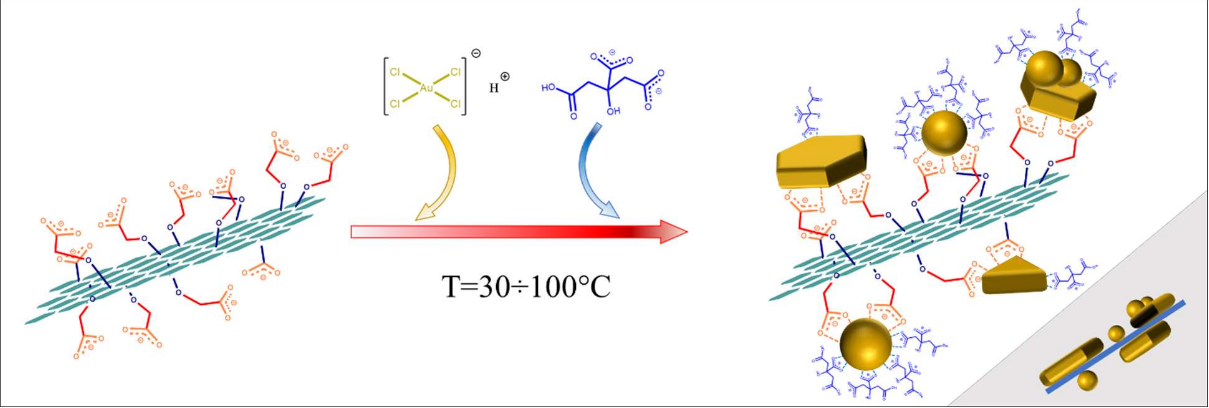

**Scheme 2**. General scheme of Au NPs heteronucleation onto the c-NGO sheets.

### 3.2.1 *Control experiments for the hybrid nanocomposite synthesis.*

A set of preliminary control experiments has been performed, to elucidate the NP growth process on c-NGO in presence of the Au precursor. The Au precursor has been added to a neat c-NGO dispersion in fresh Milli-Q water, and heated, under reflux, up to 30°C, 70°C or 100°C. The characterization of the obtained hybrid nanostructures, performed by UV-Vis-NIR absorption spectroscopy and TEM (Fig. S1 of Supplementary Material), reveals the formation of faceted Au nanostructures of similar size and size distribution onto the c-NGO sheets for all the samples, irrespectively of the investigated temperatures, being, in fact, reasonably due to spontaneous galvanic reduction, taking place by electron transfers from c-NGO to Au (III) [32].

### 3.3 Effect of sodium citrate injection order and temperature.

The synthesis has been carried out rapidly injecting sodium citrate as reducing agent into the reaction vessel already containing c-NGO and Au precursor, to investigate the effect of the chemical reduction on the Au NP heteronucleation and growth processes, with respect to the spontaneous galvanic reduction. Concomitantly, the reaction temperature effect has been studied by heating at increasing temperature (30°, 70° and 100° C) under reflux.

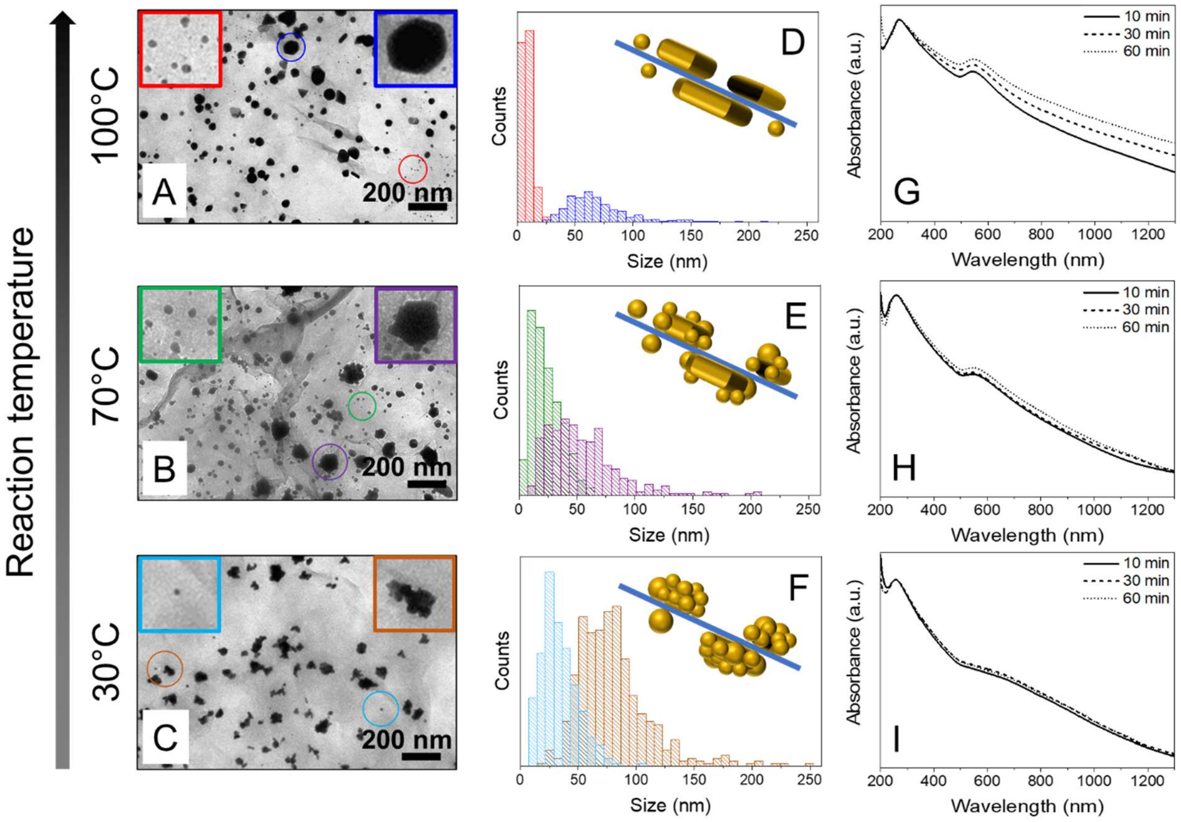

**Fig. 2.** TEM micrographs (A-C) with details of Au NPs morphology (in the insets), and Au NPs size distribution for the c-NGO/Au NPs samples obtained at 60 min of reaction with respective sketches (D-F). UV-Vis-NIR absorption spectra (G-I) of c-NGO/Au NPs obtained at 10 min (solid line), 30 min (dashed line) and 60 min (dotted line) reaction time. c-NGO/Au NPs have been synthesized with 2:1 c-NGO:Au precursor w/w ratio and 160:1 citrate:Au precursor molar ratio at 100°C (A, D and G), 70°C (B, E and H) and 30°C (C, F and I). (The sketches are not drawn to scale).

The TEM images of the samples obtained at 30°C show the presence, onto the c-NGO sheets, of both spherical and irregularly shaped Au nanostructures, with no uniform image contrast (Fig.2 Sample C), with a size ranging between 7.9-106.2 nm and 20.4-251.7 nm, respectively. Similarly, nanostructures characterized by the two distinct morphologies are observed at 70°C (Fig. 2 Sample

B), with a size between 5.0 nm and 63.0 nm, for the spherical Au NPs, and between 8.6 nm and 208.2 nm, for the irregularly shaped Au NPs.

Finally, faceted, and spherical nanostructures form at the highest tested temperature (100°C) (Fig. 2 Sample A), with an average size of 67.7 ± 25.7 nm and 8.8 ± 4.0 nm, respectively. Remarkably, no Au NPs homonucleation has been observed in the reaction solution.

It has been demonstrated that the reduction of chloroauric acid by sodium citrate is a thermodynamic process ($E^0_{citrate/Au}$= + 1.182V) [33] less favoured than galvanic reduction ($E^0_{c-NGO/Au}$= +1.382V) [34]. Therefore, when sodium citrate is injected into the c-NGO and Au precursor mixture, it can reduce only the unreacted Au precursor that will grow onto the Au nanostructures already formed by galvanic process [35].

Sodium citrate has been found to anchor, via hydrogen bonds, onto the surface oxygen moieties of c-NGO, thus offering additional coordinating sites for the *in situ* Au NPs synthesis [14], as its carboxyl groups coordinate $[AuCl_4]^-$ [36], forming, at first, a monodentate intermediate complex with the displacement of a $Cl^-$ ion, and, then, a five atoms ring complex, by interaction with the hydroxyl group of $[C_6H_5O_7]^{3-}$, followed by oxidation and decomposition of $[C_6H_5O_7]^{3-}$ in dicarboxy acetone (DCA).

Such ring complexes have been demonstrated to be involved in the heteronucleation processes occurring by reduction of the Au(III) to Au(I) complex, and in the final disproportionation of three Au(I) complexes to atomic Au(0), with formation of $[AuCl_4]^-$ as byproduct, that is then available for new oxidation processes [37]. Finally, $[C_6H_5O_7]^{3-}$ ions form complexes also with the $[AuCl_{4-x}OH_x]^-$ species, formed by $[AuCl_4]^-$ in water, leading to the monomers involved mainly in the Au NPs growth [38]. The formation of $[AuCl_{4-x}OH_x]^-$ species, starting from $[AuCl_4]^-$, has been found temperature dependent [39], as at the higher temperature a higher extent of hydroxylated $[AuCl_{4-x}OH_x]^-$ complex forms, leading to the further growth of the pre-formed Au seeds onto c-NGO [39].

In addition, the high temperature promotes the formation of highly deprotonated sodium citrate species that form complexes quickly with both $[AuCl_4]^-$ and $[AuCl_{4-x}OH_x]^-$, increasing their concentration and reactivity.

Thus, it is reasonable to infer that at high temperatures (100°C and 70°C), highly deprotonated citrate species reduce $[AuCl_4]^-$ leading to a burst of nucleation of Au seeds [39], and simultaneously form complexes with $AuCl_{4-x}OH_x$ inducing a rapid growth, also onto the nanostructures formed by galvanic reduction. This is especially effective at 100°C, thus accounting for the size distribution of the spherical Au NPs, that is significantly narrower than that of the faceted Au nanostructures and explain their higher density. On the contrary, at low temperatures (30°C), hydroxylated $[AuCl_{4-x}OH_x]^-$ species and deprotonated sodium citrate complexes form to a lower extent. Therefore, the high availability of $[AuCl_4]^-$ along with the lower efficiency of the deprotonated $Na_{3-y}C_6H_5O_7^{y-}$ in stabilizing both the monomers and the Au clusters during the growth, reduce both the monomer concentration and reactivity. The net effect is to promote inhomogeneous aggregative growth processes, which evolve by addition of monomers diffusing from the solution bulk, and by coalescence of primary NPs. Such processes may also take place onto the faceted nanostructures formed by galvanic reduction [40], thus explaining the concomitant presence of both spherical and irregular nanostructures in Sample C of Fig. 2.

| | Reaction temperature | | | | | |
|---|---|---|---|---|---|---|
| | 100 °C | | 70°C | | 30°C | |
| Reaction time (min) | π-π* transition of the -C=C- bond (nm) | LSPR peak (nm) | π-π* transition of the -C=C- bond (nm) | LSPR peak (nm) | π-π* transition of the -C=C- bond (nm) | LSPR peak (nm) |
| 10 | 269 | 541 | 261 | 545 | 257 | 646 |
| 30 | | 544 | | 547 | | 648 |
| 60 | | 546 | | 549 | | 652 |

**Table 1.** Summary of the π-π* transition positions of the -C=C- bond and of the Au NPs LSPR peak in the c-NGO/Au NPs samples obtained at 100°C, 70°C and 30°C and measured at 10, 30 and 60 min of reaction.

The UV-Vis-NIR absorption spectra of the c-NGO/Au NPs hybrid nanostructures, prepared at the different investigated temperatures, show, for all the samples, a peak in the UV region ascribed to the π-π* transition of the -C=C- bond of c-NGO, that shifts towards higher wavelengths as the reaction temperature increases (Fig. 2G-I). Such a bathochromic shift can be accounted for by the reduction of NGO induced by sodium citrate addition [14], and its increase with temperature can be due to the formation of higher deprotonated citrate species, that more efficiently reduce GO [14]. In the same spectra, the characteristic Localized Surface Plasmon Resonance (LSPR) band of the Au NPs, originated from collective excitation of the free conduction band electrons [41], is observed at 646 nm, 545 nm and 541 nm, respectively at 30, 70, 100°C, after 10 min from injection of sodium citrate (Fig. 2G-I). Such a shift towards the higher energy side, and the concomitant decrease of the LSPR band width with the increase of the reaction temperature, can be ascribed both to a narrowing of the Au NPs size distribution and to a decrease of the Au NPs/c-NGO electron coupling [42].

The time evolution of Au NPs LSPR peak and of the c-NGO sheets coverage density has been investigated also at longer reaction time (30 and 60 min) after sodium citrate injection. The results show a progressive increase in intensity and a red shift (Fig. 2G-I, Table 1), reasonably due to the slow Au NPs growth by addition of Au monomer species ($[AuCl_{4-x}OH_x]^-$) diffusing from the solution bulk [41].

Moreover, the TEM analysis (Fig. S2) of the samples achieved at 100°C at increasing reaction time shows no significant difference in sheets coating density (Fig. S2). In contrast, the Au NPs size increases up to 10% after 60 min. A similar trend is observed for the samples prepared at 70°C and 30°C and these results confirm that the citrate injection into the c-NGO and Au precursor reaction mixture induces reduction of the unreacted precursor. Finally, spectroscopy and microscopy investigation performed on samples obtained at higher reaction times, up to 2 h, does not show any significant changes of the LSPR peak position and of the mean Au NP size (data not shown), thus assessing the completion of the Au precursor reaction after 60 min.

### 3.4 Effect of the Au precursor and sodium citrate injection order.

The observed interplay between galvanic and sodium citrate induced Au reduction has prompted the investigation of the effect of Au precursor and sodium citrate injection into the c-NGO starting dispersion, on the reaction mechanism and on the resulting nanostructure properties.

For this purpose, the c-NGO/Au NPs hybrid nanocomposite has been synthesized at 100°C, under reflux, injecting sodium citrate into the reaction flask already containing c-NGO in Milli-Q water, and subsequently fast injecting the Au precursor. Such an experiment has been performed using 160:1 sodium citrate:Au precursor molar ratio, 2:1 c-NGO:Au precursor w/w and pH 6.83 c-NGO starting dispersion. Spectroscopic and morphological properties of the achieved sample (Fig. 3A-H) are comparable with those of Sample A of Fig. 2, synthesized in the same experimental conditions, but by inverting the injection order.

The TEM images show that the c-NGO sheets are densely coated by high contrast, spherical Au NPs, with small mean size and narrow size distribution (Fig. 3A). The results indicate that the inverted injection order of reactants can mitigate the galvanic process, slowing down the NPs growth and granting higher monodispersion. Therefore, such an injection order has been used for further experiments.

### 3.5 Effect of the pH of the c-NGO starting dispersion.

c-NGO/Au NPs has been synthesized by injecting the Au precursor in an aqueous dispersion of citrate and c-NGO. The higher extent of c-NGO sheets exfoliation and their higher colloidal stability at pH 11 (Fig. 1D) have prompted the use of such a pH in the starting dispersion.

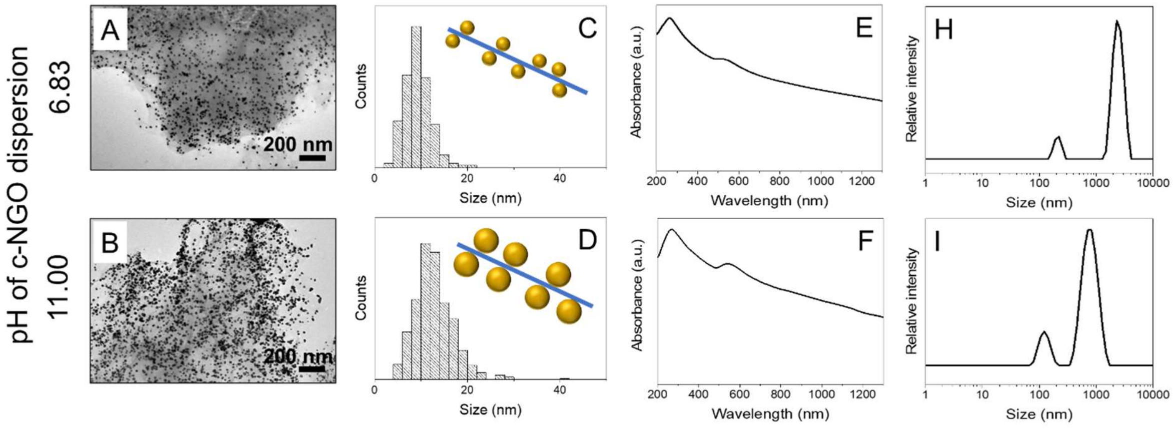

**Fig. 3.** TEM micrographs (A-B), NPs size distribution with related sketch of the Au NP decorated c-NGO samples (C-D), UV-Vis-NIR absorption spectra (E-F) and DLS traces (H-I) of c-NGO/Au NPs at 60 min reaction time, with the 2:1 c-NGO:Au w/w ratio, 160:1 citrate:Au precursor molar

ratio, reaction temperature of 100°C and pH of the c-NGO dispersion of 6.83 (A-H) and 11 (B-I). (The sketches are not drawn to scale).

In this condition, the Au NPs have a size of 12.8 ± 4.2 nm (Fig. 3D), slightly larger than that of the NPs synthesized in the c-NGO starting dispersion at pH 6.83, that is 9.2 ± 2.8 nm (Fig. C).

The UV-Vis-NIR absorption spectra of the nanocomposites synthesized at pH 11 show the c-NGO -C=C- $\pi$-$\pi^*$ transition peak at 266 nm (Fig. 3E-F), red shifted with respect to that at 257 nm of the pristine c-NGO (Fig. S1G). In addition, the LSPR band at 532 nm, in the spectrum of Sample A (Fig. 3), shifts up to 540 nm in that of Sample B, thus accounting for the larger NPs mean size measured in the TEM micrographs (Fig. 3A-B).

Such a feature can be likely ascribed to the shift of the reaction equilibrium of the Au species towards the formation of $[AuCl_{4-x}OH_x]^-$ and of highly deprotonated citrate species, that form very quickly highly reactive complexes [39].

The TEM micrograph of the samples prepared at pH 11 presents the same coating density and a Au NPs dimension almost independent of the reaction time (12.1±5.4 nm, 12.3±3.6 nm and to 12.8±4.2 nm after 10 min, 30 min and 60 min, respectively) (Fig. S3) suggesting that fast reaction kinetics between $[AuCl_{4-x}OH_x]^-$ and highly deprotonated citrate species ($Na_{3-y}C_6H_5O_7^{y-}$) result in a fast NPs growth already in the first 10 min of reaction.

DLS signal of the nanocomposite synthesized at pH 6.83 shows a bimodal size distribution with the population at 220±2 nm (Fig. 3H), reasonably ascribed to few layers c-NGO decorated by citrate-coordinated Au NPs. A second population, at 2305±16 nm (PDI=0.806±0.026), can be ascribed to larger c-NGO/Au NPs aggregates. On the other hand, the DLS signal recorded for the sample at pH 11 shows a shift of both the populations towards smaller hydrodynamic size, namely 124±2 nm and 798±5 nm (PDI=0.748±0.015), respectively. Due to the lower aggregation of the nanocomposites obtained under this condition, the further systematic investigation of the material properties has been performed by injecting the Au precursor in a dispersion of citrate added to the pH 11 c-NGO starting dispersion.

### 3.6 Effect of citrate:Au precursor molar ratio.

Another set of experiments has been performed by varying citrate:Au precursor molar ratio (80:1, 160:1 and 320:1), keeping constant Au precursor concentration, c-NGO:Au precursor molar ratio at 2:1 and pH of the c-NGO starting dispersion (pH 11).

TEM images of the achieved structures show c-NGO sheets highly densely coated by spherical Au NPs (Fig. 4A-C) having comparable mean sizes, and the occurrence of aggregative Au NPs growth phenomena both at high and low citrate:Au precursor molar ratio (Fig. 4A and C). These results can be explained considering the role of citrate in controlling the ionic strength of the reaction solution. At the 80:1 molar ratio, the low concentration of citrate is ineffective in stabilizing the Au seeds, and hence, aggregation occurs (Fig. 4A). Conversely, at the 320:1 molar ratio, the high citrate concentration is responsible of a high ionic strength in the reaction environment. According to Derjaguin-Landau-Verwey-Overbeek (DLVO) theory, that considers the colloidal NPs dispersed in aqueous media having a surface potential given by the sum of the repulsive electrostatic forces and Van der Waals attractive contribution, a high ionic strength may provide Van der Waals attractive interactions, higher with respect to the repulsive ones, leading to aggregation of heteronucleated NPs [43,44] Fig. 4C).

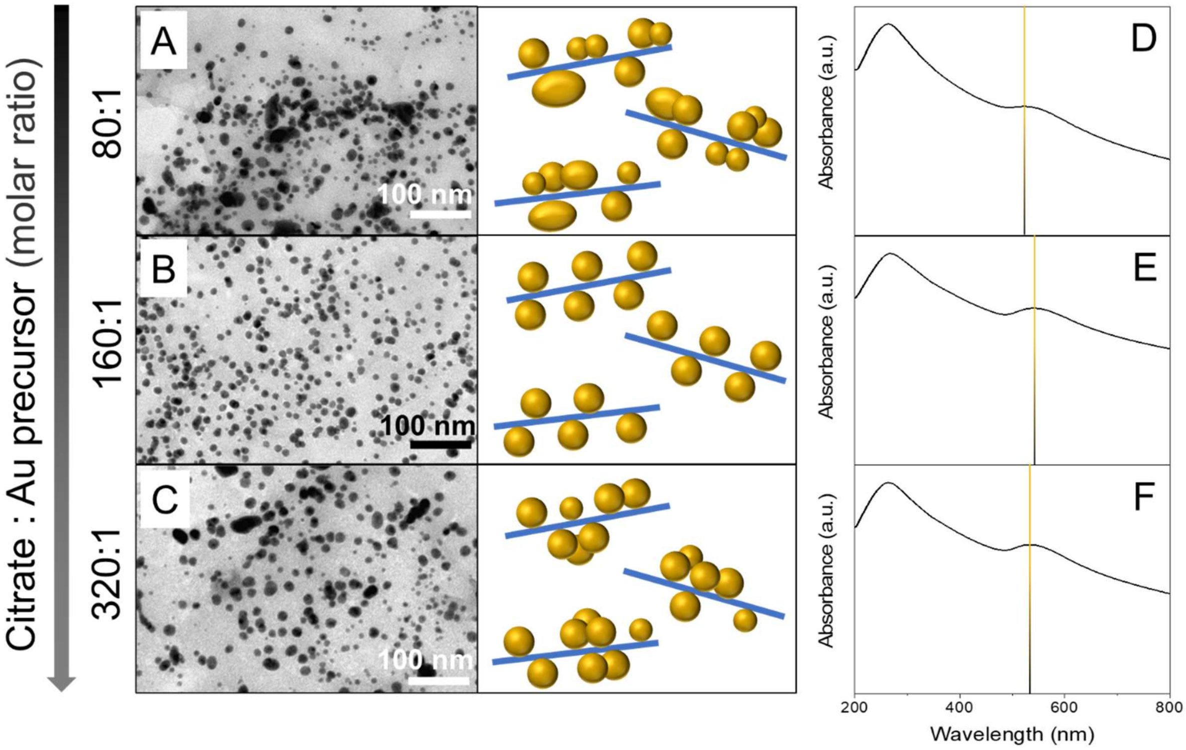

**Fig. 4.** TEM micrographs with related sketch (A-C) and UV-Vis-NIR absorption spectra (D-F) of c-NGO/Au NPs samples synthesized at 100°C, at 60 min reaction time, with 2:1 c-NGO:Au precursor w/w ratio and 80:1 (A and D), 160:1 (B and E) and 320:1 (C and F) citrate:Au precursor molar ratio. (The sketches are not drawn to scale).

The nanocomposites present the -C=C- peak of c-NGO at 265 nm and the LSPR peak of the Au NPs at 521 nm, 540 nm and 533 nm, when obtained with the 80:1, 160:1 and 320:1 molar ratio, respectively, showing a red shift at increasing Au NPs size, [45] likely due to the different chemical environment surrounding the NPs and their different aggregation extent [46] (Fig. 4D-F).

Considering the higher Au NPs monodispersion, the sample synthesized with the 160:1 citrate:Au precursor molar ratio has been selected for further investigation.

### 3.7 Effect of the c-NGO: Au precursor w/w.

The morphology and size distribution of the Au NPs have also been investigated by varying c-NGO:Au precursor w/w (0.25:1, 0.5:1, 1:1, 2:1 and 3:1), and keeping fixed the citrate:Au precursor molar ratio (160:1) and the pH of the c-NGO starting dispersion (pH 11).

The TEM images in Fig. 5A-E show an almost constant average Au NPs size of ca. 12.8 nm in the samples achieved with the 0.25:1, 0.5:1, 1:1 and 2:1 w/w ratio, which decreases down to ca. 7.9 nm for the sample with the 3:1 c-NGO:Au precursor w/w ratio. In addition, an enhancement of the coating density with the decrease of the c-NGO:Au precursor w/w is observed.

The narrowing of the NPs size distribution and the decrease of the Au NPs mean size at increasing c-NGO:Au precursor w/w ratio can be reasonably ascribed to the larger amount of the $-COO^-$ moieties available onto the sheets, which behave as coordinating sites for the Au NPs, thus assisting and directing the NPs heteronucleation, finally determining their size. Therefore the $[AuCl4]^-$ species bind to the larger number of $-COO^-$ groups, leading to a higher number of rapid and discrete heteronucleation events, that are followed by a slow, thermodynamically controlled, isotropic growth of Au seeds, fed by the available monomers diffusing from the solution bulk. Therefore, a high number of smaller NPs heteronucleate onto the c-NGO sheets, resulting in a high coating density [42].

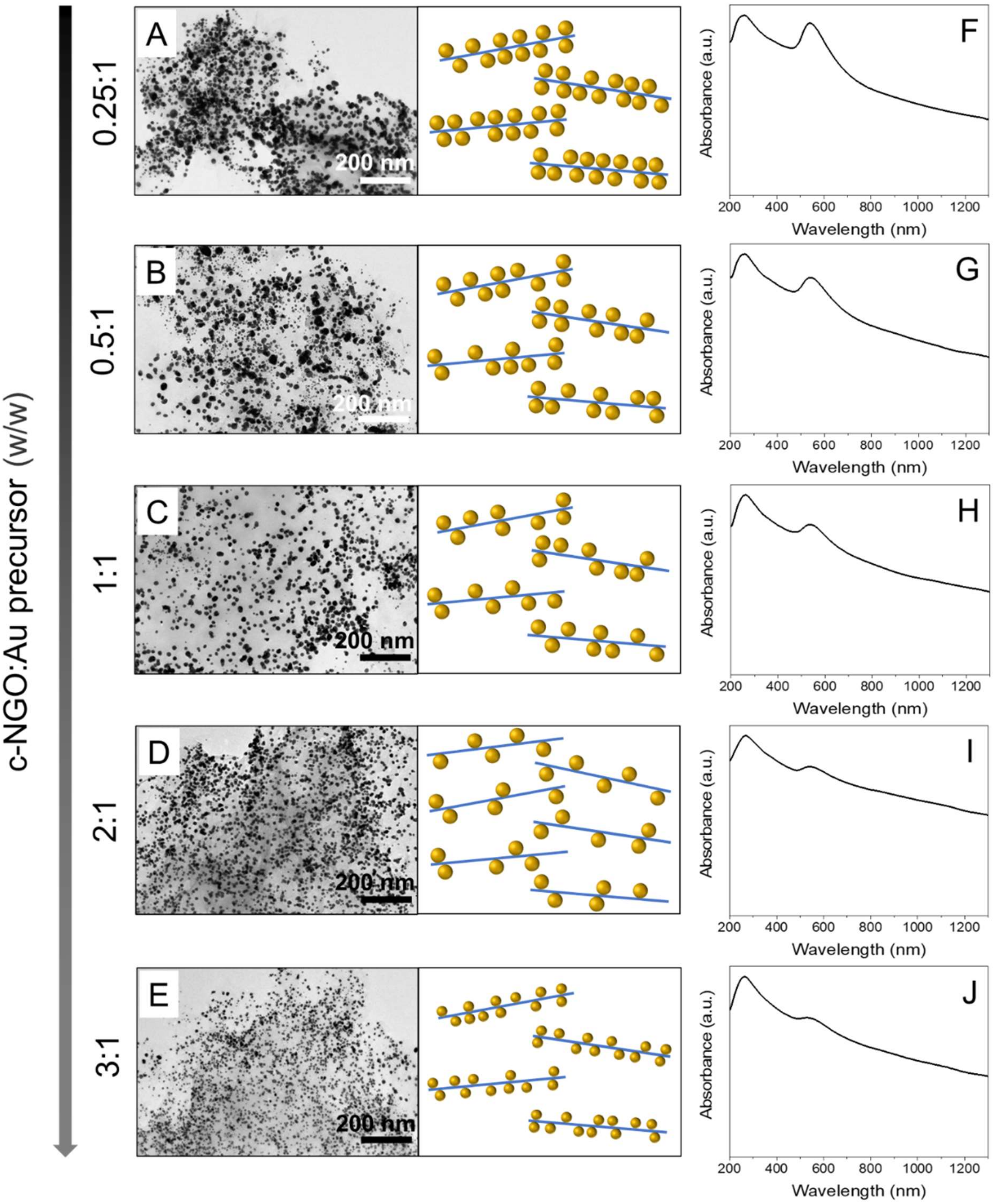

**Fig. 5.** TEM micrographs with related sketches (A-E) and UV-Vis-NIR absorption spectra (F-J) of c-NGO/Au NPs, synthesized with the 160:1 citrate:Au precursor molar ratio and 0.25:1 (A and F), 0.5:1 (B and G), 1:1 (C and H), 2:1 (D and I) and 3:1 (E and J) c-NGO:Au precursor w/w ratio, at 100°C and 60 min reaction time. (The sketches are not drawn to scale).

In the UV-Vis-NIR absorption spectra (Fig. 5F-J), the LSPR peak shifts towards the higher energy side of the spectrum with the increase of the Au NPs average size, namely it is 543 nm for the 0.25:1, 0.5:1, 1:1 and 2:1 w/w ratio samples and 528 nm for the 3:1 w/w one.

It is worth noticing that isolation experiments performed by centrifuging, under the same conditions, in their reaction mixtures, c-NGO/AuNPs and neat citrate coated Au NPs having size comparable to that of the NPs decorating the c-NGO basal plane (Fig. S4), have accounted for the effectiveness of the Au NPs anchoring onto the chemically grafted -COOH moieties of the c-NGO sheets, without any Au NPs homonucleation phenomena (Fig. S4).

Raman spectra of the hybrid nanostructures synthesized with the 0.25:1 c-NGO:Au precursor w/w compared with the spectrum of neat c-NGO (Fig. S5) do not show any changes either in intensity and position of the G peak at 1600 $cm^{-1}$, indicating retention of the structural properties of c-NGO after formation of the Au NPs.

It is worth noticing, that the coverage of the c-NGO/Au NPs nanocomposite synthesized with 0.25:1 and 0.5:1 c-NGO:Au precursor w/w ratio, exceeds that reported for similar nanocomposites based on NGO and Au NPs [14,18,19], and also shows a narrow and reproducible Au NPs dispersion. Due to the high coating density, both the 0.25:1 and 0.5:1 c-NGO:Au precursor w/w ratio samples have been considered for the further investigation.

### 3.8 Functionalization of c-NGO/Au NPs with HS-PEG.

The c-NGO/Au NPs samples obtained with the 0.25:1 and 0.5:1 c-NGO:Au precursor w/w ratio have been functionalized with HS-PEG, to improve the nanocomposite dispersion in aqueous media and convey to the materials the stealth properties of the polymer. Since citrate only weakly binds the Au NP surface (6.7 kJ $mol^{-1}$) [24], it can be easily exchanged with HS-PEG, that binds the thiol groups to the Au NPs surface by means of a stronger covalent bond (188 kJ $mol^{-1}$) [47] (Scheme 3).

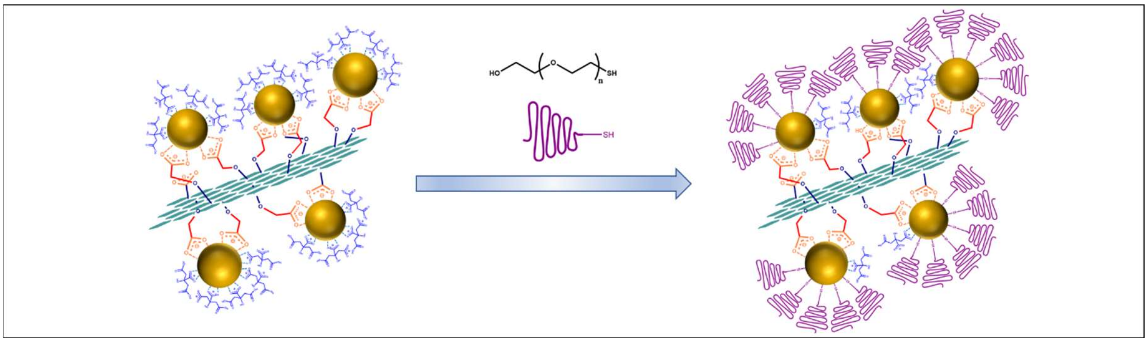

**Scheme 3.** Sketch of the functionalization of c-NGO/Au NPs with HS-PEG.

The nanocomposites have been functionalized by adding, under stirring, HS-PEG aqueous solutions, prepared at different c-NGO:HS-PEG w/w ratio (namely 1:1, 1:5, 1:10, 1:15 and 1:30), and then, performing a dialysis step for purifying samples from the excess of HS-PEG.

DLS measurements of the nanocomposites treated with HS-PEG at different c-NGO:HS-PEG w/w reveal an increase of the dispersibility at decreasing w/w ratio (Fig. S6), as confirmed by their hydrodynamic size decrease (Table 2).

| c-NGO:HS-PEG (w/w) | 0.5:1 c-NGO:Au precursor w/w | | | 0.25:1 c-NGO:Au precursor w/w | | |
|---|---|---|---|---|---|---|
| | $D_{h,mean}$ (nm) | PolyDispersity Index (PDI) | ζ-potential (mV) | $D_{h,mean}$ (nm) | PolyDispersity Index (PDI) | ζ-potential (mV) |
| 1:1 | 344±1 | 0.441±0.008 | -57.5±2.2 | 262±5 | 0.399±0.018 | -53.0±5.5 |
| 1:5 | 286±3 | 0.416±0.022 | -56.7±0.7 | 245±3 | 0.388±0.002 | -50.4±0.4 |
| 1:10 | 193±4 | 0.336±0.029 | -48.0±0.8 | 153±1 | 0.384±0.022 | -36.2±0.9 |

**Table 2.** Summary of the intensity-average hydrodynamic diameter ($D_{h,mean}$) and corresponding polydispersity index (PDI) determined by DLS and ζ-potential value of c-NGO/Au NPs achieved with 0.5:1 and 0.25:1 c-NGO:Au precursor w/w, functionalized with HS-PEG at 1:1, 1:5 and 1:10 c-NGO:HS-PEG w/w.

The obtained results indicate an improved dispersion of both the nanocomposites with a maximum for the 1:10 c-NGO:HS-PEG w/w ratio sample (Table 2), induced by hydrophobic interactions that allow PEG chains intercalation between c-NGO sheets, thus limiting their $\pi$-$\pi$ stacking [48]. Lower c-NGO:HS-PEG w/w ratio samples, namely 1:15 and 1:30, have also been investigated, but both nanocomposites hydrodynamic size and colloidal stability have been found not to significantly change with respect to the 1:10 c-NGO:HS-PEG w/w sample (data not shown).

On the other hand, the ζ-potential value decreases at decreasing c-NGO:HS-PEG w/w ratio (Table 2), reasonably due to the displacement, at the NPs surface, of the negatively charged citrate ligand by neutral HS-PEG and concomitant shielding effect of its chains on negative citrate charges.

After HS-PEG functionalization, the absorption spectra of the samples (Fig. S6E-G and K-M) show a slight increase of the absorbance intensity of the c-NGO peak at 257 nm, due to the overlap of the $\pi$-$\pi^*$ transition signal with the $n$-$\pi^*$ transition peak of the HS-PEG -C-S- bond [49] at ca. 230 nm, whilst no shift of the Au NPs LSPR peak is observed.

ATR-FTIR spectra of the c-NGO/Au NPs-PEG and c-NGO/Au NPs samples, compared to those of bare c-NGO, sodium citrate and HS-PEG (Fig. S7) show a decrease of the intensity of the -C=O stretching at 1723 cm$^{-1}$ and an increase of the asymmetric stretching of the -COO$^-$ groups at 1562 cm$^{-1}$ with respect to the spectrum of the neat c-NGO, likely due to the presence of citrate coordinating the Au NPs surface. The spectrum of the HS-PEG functionalized sample exhibits the characteristic vibrations of the -CH$_2$-CH$_2$-O- moieties of PEG at 1146 cm$^{-1}$, 1102 cm$^{-1}$ (both $\nu_{as\text{-}COC\text{-}}$) and 1059 cm$^{-1}$ ($\nu_{s\text{-}COC\text{-}}$) [50], indicating the effective binding of the polymer, and explaining its high dispersibility in aqueous media, as well as its long-term colloidal stability.

### 3.9 Theoretical determination of Au NPs coating density onto c-NGO sheets.

An original theoretical approach has been implemented for estimating the Au NPs coating density of the c-NGO sheets, by exploiting experimental data achieved from TEM and DLS measurements.

The calculation starts from the assumption that the total volume ($V_{tot}$) of c-NGO used in the reaction, stays constant, and that the c-NGO sample is composed of *i* populations of sheets having *i* different size. Therefore, $V_{tot}$ will be the sum of partial volumes $V_{part,i}$ of populations of NGO which can be written as the number of the c-NGO sheets $N_i$, multiplied by the volume of the single c-NGO sheets $V_{s,i}$:

$$V_{tot} = \sum_i V_{part,i} = \sum_i N_i \cdot V_{s,i} \tag{1}$$

where $V_{tot}$ can be considered as sum of volume fraction $\kappa_i$ occupied by population *i*, which can be obtained by DLS data, multiplied by $V_{tot}$:

$$V_{tot} = \sum_i \kappa_i \cdot V_{tot} \tag{2}$$

with $\sum_i \kappa_i = 1$.

Therefore, the total number $N_{NGO,tot}$ of $N_i$ sheets is obtained by equaling Eq. (1) with Eq. (2), and finally as:

$$N_{NGO,tot} = \sum_i N_i = \sum_i \frac{\kappa_i \cdot V_{tot}}{V_{s,i}} \tag{3}$$

where $V_{tot}$ can be calculated from the c-NGO mass $m_{NGO}$ used in the reaction:

$$V_{tot} = \frac{m_{NGO}}{\rho_{NGO}} \tag{4}$$

and $\rho_{NGO}$ is the c-NGO density (0.44 g $cm^{-3}$) [51].

TEM images show quadrangular-shaped c-NGO sheets (Fig. 1A), whilst DLS provides typically a hydrodynamic size distribution of spherical NPs. Assuming a square-like morphology of the sheets, the c-NGO flakes are considered inscribed in a circumference representing the geometrical projection of the sphere in the DLS model, with $L_i$, the circumference diameter corresponding to the square diagonal. Therefore, volume of a single c-NGO sheet is:

$$V_{s,i} = A_i h = \left( \frac{L_i}{\sqrt{2}} \right)^2 \cdot h = \frac{L_i^2 h}{2} \tag{5}$$

where $A_i$ and $h$ are area and thickness of c-NGO, respectively.

The hydrodynamic diameter $D_{H,i}$ measured by DLS is related to $L_i$ through the following relation [21]:

$$D_{H,i} = \sqrt[3]{\frac{3}{16} h L_i^2} \tag{6}$$

valid if $h \ll L_i$. The insertion of Eq.s (4), (5) and (6) into Eq. (3) allows to obtain $N_{NGO,tot}$ only in function of experimental data:

$$N_{NGO,tot} = \frac{3}{8} \frac{m_{NGO}}{\rho_{GO}} \sum_i \frac{\kappa_i}{D_{H,i}^3} \tag{7}$$

It is worth noticing that the proposed approach is independent on the thickness $h$ of the c-NGO sheet, and hence, it does not consider the exfoliation degree.

Assuming the Au NPs as spheres having the size distribution obtained by the TEM images, the $\eta_i$ fraction of Au NPs with size $d_i$ can be expressed as the ratio between the number of Au NPs $\xi_i$ with size $d_i$ and the total number of Au NPs, expressed as sum of Au NP $\xi_i$ with a relative diameter $d_i$:

$$\eta_i = \frac{\xi_i}{\sum_i \xi_i} \tag{8}$$

with $\sum_i \eta_i = 1$. Therefore, the total number of Au NPs $N_{NP,tot}$ will also be given by:

$$N_{NP,tot} = \sum_i \eta_i N_{NP,tot} \tag{9}$$

where $V_{NP,tot}$, the total volume of Au NPs, will result by the number of Au NPs times the volume of a single Au NP $V_{NP,s,i}$:

$$V_{NP,tot} = \sum_i \eta_i N_{NP,tot} V_{NP,s,i} \tag{10}$$

where $V_{NP,s,i} = \frac{4}{3}\pi\left(\frac{d_i}{2}\right)^3$ and thus, $N_{NP,tot}$ can be extracted rewriting equation (10) as:

$$N_{NP,tot} = \frac{V_{NP,tot}}{\frac{\pi}{6}\sum_i \eta_i d_i^3} \tag{11}$$

As homonucleation of Au NPs has not been observed in the investigated reactions, the heteronucleation of the Au precursor can be assumed quantitative. Hence, $V_{NP,tot}$ can be easily computed as the ratio between the amount of tetrachloroauric acid ($m_{HAuCl_4 \times 3H_2O}$) used in the reaction, and the density of metallic Au ($\rho_{Au}$=19.3 g cm$^{-3}$). The amount of Au ($m_{Au}$) synthesized by redox decomposition of the Au precursor by citrate is calculated from the moles of Au precursor:

$$m_{Au} = \frac{m_{HAuCl_4 \times 3H_2O}}{w_{HAuCl_4 \times 3H_2O}} w_{Au} \tag{12}$$

where $w_{HAuCl_4 \times 3H_2O}$ and $w_{Au}$ are the molecular and atomic weight of Au precursor and Au, respectively.

By equating the Eq.s (11) and (12), the mathematical expression of $N_{NP,tot}$ can be obtained by using only experimental data:

$$N_{NP,tot} = \frac{m_{HAuCl_4 \times 3H_2O} w_{Au}}{\frac{\pi}{6}\rho_{Au} w_{HAuCl_4 \times 3H_2O} \sum_i \eta_i d_i^3} \tag{13}$$

Finally, the average number of Au NPs per NGO sheet $N_c$ is defined as ratio between the total number of Au NPs and the total number of dispersed c-NGO sheets:

$$N_c = \frac{N_{NP,tot}}{N_{NGO,tot}} \tag{14}$$

and, thus, the results are related to the coating density.

When this approach is applied to the samples investigated in Fig. 5, it results in an average number of dozen of Au NPs decorating the c-NGO sheets that increase with c-NGO:Au precursor w/w decrease (namely 33.2 for 2:1 w/w, 45.1 for 1:1 w/w, 74.3 for 0.5:1 w/w and 97.9 for 0.25:1 w/w), as assessed by the Au NPs/c-NGO absorption intensity ratio of Fig. 5 F-J. The 3:1 w/w ratio sample results in a $N_c$ of 65.9, reasonably explained by the high amount of -COO$^-$ sites on the c-NGO sheets, where the Au precursor can heteronucleate, ultimately resulting in a high value of $N_{NP,tot}$ Au NPs with smaller $d_i$.

### 3.10 Investigation of the photothermal properties of the hybrid nanocomposites.

The photothermal conversion ability of the c-NGO/Au NPs samples, synthesized with the 160:1 citrate:Au precursor molar ratio, 0.25:1 c-NGO:Au precursor w/w ratio and with pH 11 c-NGO starting dispersion, and of the c-NGO/Au NPs-PEG sample, prepared with 1:10 c-NGO:HS-PEG w/w ratio, has been investigated under irradiation with two CW laser beams emitting at 532 nm and 808 nm, respectively. The absorbance spectra of the samples are reported in Figure S8 for comparison. The green laser ($\lambda$=532 nm) has been used to selectively investigate the photothermal response of the Au NPs heteronucleated onto the c-NGO surface. The experimental results obtained by analyzing the thermal images acquired with the thermo-optical setup sketched in Scheme 2, are reported in Fig. 6. Fig. 6A-B show that, by keeping constant the laser intensity (I) at 21 W·cm$^{-2}$, c-NGO/Au NPs (panel A) and c-NGO/Au NPs-PEG (panel B) lead to a gradual temperature increase ($\Delta$T) of 16.20 °C (panel A) and 20.00°C (panel B), respectively during first 2 min irradiation. For both samples, maximum $\Delta$T values, measured at end of pump beam irradiation, increase linearly with laser beam power intensity (Fig. 6C-D), in agreement with theoretical models [52] and experimental results [53] reported in detail elsewhere.

Furthermore, as control experiment, photothermal behavior of bare c-NGO has been also investigated at same laser intensity (I = 21 W $cm^{-2}$) (Fig. S9A), resulting in a $\Delta T$ of 13.40 °C after 2 min of irradiation. It is worthwhile noticing that, in same experimental conditions, $\Delta T$ values measured for c-NGO/Au NPs and c-NGO/Au NPs-PEG are, respectively, 1.2 and 1.5 times higher than the temperature increase of c-NGO. Such a difference in photothermal responses can be associated with the extraordinary ability of Au NPs to convert light into heat [54,55]. Notably, for all the investigated ranges of laser power intensity, the $\Delta T$ values obtained from c-NGO/Au NPs-PEG are higher than the temperature increase produced by c-NGO/Au NPs. As an example, at 17 $W \cdot cm^{-2}$, a $\Delta T$ of 12.01°C is measured for c-NGO/Au NPs, while a $\Delta T$ of 17.55 °C is obtained by irradiating c-NGO/Au NPs-PEG, which turns out to be about 5°C higher.

In addition, as reported in Fig. S8, the LSPR band in the spectrum of the c-NGO/Au NPs-PEG heterostructure exhibits a higher absorption intensity with respect to that recorded for the c-NGO/Au NPs nanocomposite, for samples at the same c-NGO concentration. These evidences can be associated with the dielectric and thermal properties of the PEG layer that produces an increase of the photothermal efficiency [56].

Fig. 6E reports the spatial temperature distribution as function of the position along the side wall of the quartz cuvette exposed to the green laser beam. Experimental results have been obtained elaborating thermographic images collected after 120 s of laser irradiation, from regularly spaced points along the black line segment, reported in Fig. 6 F-G (red outlined images). The corresponding thermographic images are reported on the right side of panel F, for c-NGO/Au NPs, and of panel G, for c-NGO/Au NPs-PEG.

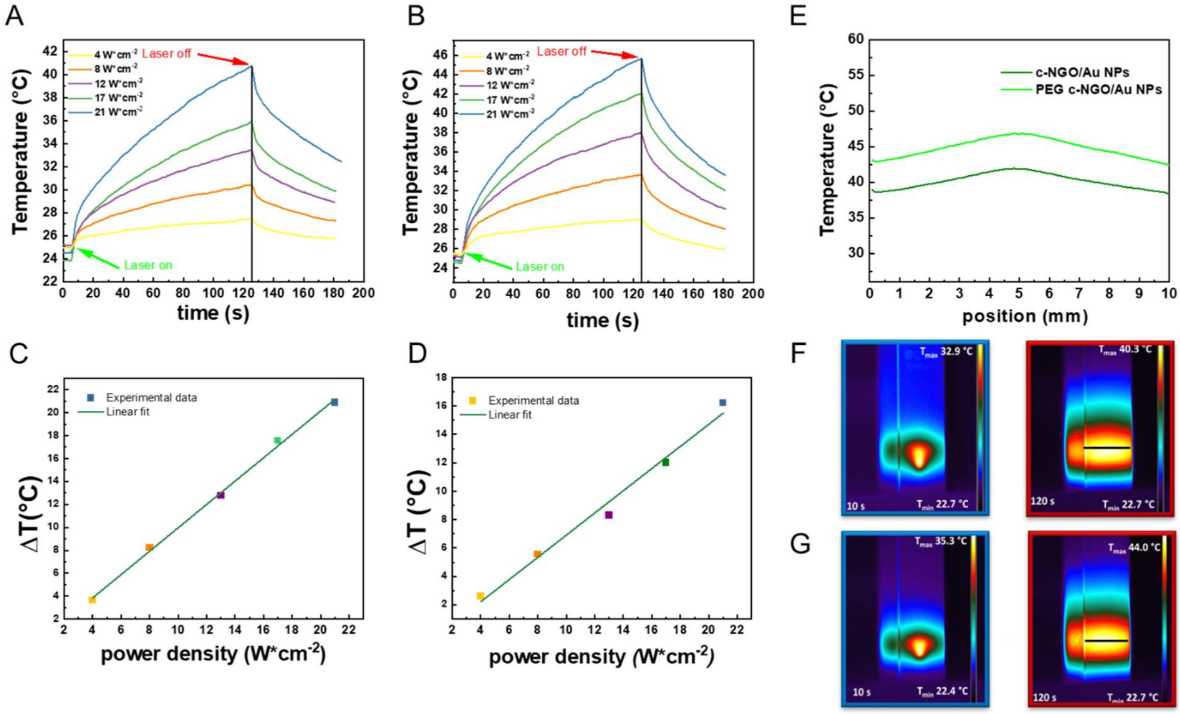

**Fig. 6.** Results of the spatial-temporal photothermal experiments performed under a CW pump beam irradiation (λ=532 nm). Time-temperature dependence recorded for the c-NGO/Au NPs (A) and c-NGO/Au NPs-PEG (B) samples along with the corresponding linear fit of the average temperature variations (C) and (D) at the different values of the laser beam intensity. Spatial-temperature profiles of c-NGO/Au NPs and c-NGO/Au NPs-PEG (E) after 120 s of irradiation obtained from regularly spaced points along the black line segment reported in the thermographic images (F) and (G) (right images). Representative thermographic images of c-NGO/Au NPs (F) and c-NGO/Au NPs-PEG (G) acquired after 10 s (left) and 120 s (right) of continuous laser irradiation (I=21 W $cm^{-2}$). All experiments have been performed on a 45µg $mL^{-1}$ aqueous dispersion.

The thermographic images are color maps reproducing the temperature values measured by the thermal camera according to the selected color palette. The left side of Fig. 6F-G highlights that, after 10 s of laser irradiation, the highest temperature value is reached only in the area of the cuvette irradiated by the laser spot. On the contrary, as shown in the right side of Fig. 6 F-G, after 120 s of irradiation, the produced heating is uniformly distributed over a wider area. Indeed, the spatial-temperature curves reported in Fig. 6E point out a uniform distribution of heat collected along the side of the cuvette exposed to the thermal camera, thus indicating a homogenous spatial distribution of the thermoplasmonic heating inside the cuvette at the end of the experiment. As reported in Fig. S8, the absorption spectra of c-NGO/Au NPs and c-NGO/Au NPs-PEG samples show an absorption intensity higher than that of bare c-NGO, in the 700-1300 nm range.

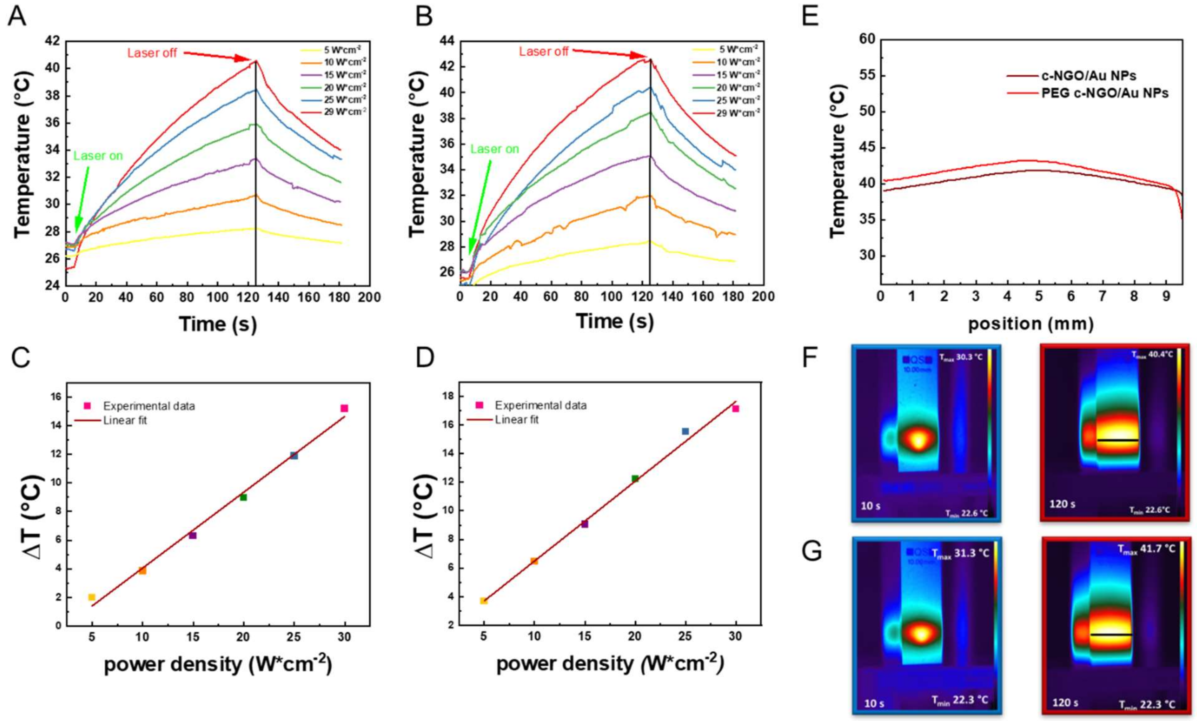

**Fig. 7.** Results of the spatial-temporal photothermal experiments performed under a CW pump beam irradiation ($\lambda$=808 nm). Time-temperature dependence of c-NGO/Au NPs (A) and c-NGO/Au NPs-PEG (B) samples along with corresponding linear fit of average temperature variations (C) and (D) at different values of laser beam intensity. Spatial-temperature profiles of c-NGO/Au NPs and c-NGO/Au NPs-PEG after 120 s of irradiation obtained from regularly spaced points along the black line segment reported in thermographic images (F) and (G) (right images). Representative thermographic images of c-NGO/Au NPs (F) and c-NGO/Au NPs-PEG (G) acquired after 10 s (left) and 120 s (right) of continuous laser irradiation (I=29 W·cm$^{-2}$). All experiments were performed at 45µg mL$^{-1}$ aqueous dispersion.

Interestingly, this wavelength range encompasses the first physiological "biological window" (700-900 nm), thus allowing the suitable laser light to propagate into tissues with a penetration depth higher than 3 mm, ideal for performing PTT-assisted cancer treatments [57]. To verify this opportunity, experiments have been repeated on c-NGO/Au NPs and c-NGO/Au NPs-PEG by using a Near Infrared (NIR) laser beam ($\lambda$=808 nm). Experimental results reported in Fig. 7 C-D, show that under NIR laser irradiation ($I$=29 W·cm$^{-2}$), c-NGO/Au NPs and c-NGO/Au NPs-PEG generate a $\Delta T$ of 15.20°C and 17.30°C, respectively. Control experiments performed in the same experimental conditions on c-NGO, at the same concentration of c-NGO/Au NPs and c-NGO/Au NPs-PEG, produce a $\Delta T$ of 13.98°C (Fig. S9B). As reported in Fig. 7C-D, under NIR irradiation, $\Delta T$ exhibits the same linear dependence as function of the laser intensity. However, the photothermal investigation points out that c-NGO/Au NPs and c-NGO/Au NPs-PEG samples, although not exhibiting a plasmon band in the NIR region of the electromagnetic spectrum (Fig. S8), are able to convert NIR light into heat, producing a temperature increase higher than that observed in the control experiments (Fig. S9B). This result suggests a synergistic photothermal behavior involving the interactions between the plasmonic Au NPs and NGO, in agreement with the experimental results reported in [11, 28, 58].

The spatial-temperature curves reported in Fig. 7E have been obtained by elaborating thermographic images from regularly spaced points along the black line segment, as reported in Fig. 7 F-G (red outlined images), along with the corresponding thermographic images for c-NGO/Au NPs and c-NGO/Au NPs-PEG, respectively, highlighting that after 2 min of NIR irradiation, a uniform heating distribution is achieved. These evidences demonstrate the great potential of c-NGO/Au NPs and c-NGO/Au NPs-PEG as photothermal agents for both deep and uniform tumor ablation.

The photothermal stability of the c-NGO/Au NPs-PEG sample, which exhibits the best photothermal properties (Fig. 6B and Fig. 7B) at a concentration of 45 mg mL$^{-1}$, has been assessed by thermoplasmonic experiments by turning on and off the pump laser beams emitting at 532 nm and 808 nm, with a power density of 21 W·cm$^{-2}$ and 29 W·cm$^{-2}$, respectively, for five consecutive irradiation cycles under different irradiation/cooling times (Table S1). The results highlight its excellent photothermal stability under green and NIR laser source irradiation, respectively, even after prolongated irradiation (Fig. S10-S11).

Finally, the photothermal conversion efficiency η of both c-NGO/Au NPs and c-NGO/Au NPs-PEG has been evaluated from the τ, time constant values, which have been estimated by the cooling phase of the time-temperature plots (Fig. 6 A-B and Fig. 7 A-B), in agreement with the Roper model [57]. Under green laser light irradiation, the c-NGO/Au NPs-PEG sample shows a τ of 41 s, while c-NGO/Au NPs displays a τ of 103 s (Table S2). Accordingly, the photothermal conversion efficiency of c-NGO/Au NPs-PEG is expected to be higher than c-NGO/Au NPs. Such a behavior endorses the higher ΔT value of c-NGO/Au NPs-PEG (20.00°C, Fig. 6C) with respect to the ΔT value (16.20°C Fig. 6D) of c-NGO/Au NPs, and it can be explained considering that, for the same c-NGO concentration, the LSPR band in c-NGO/Au NPs-PEG exhibits a higher absorption intensity with respect to c-NGO/Au NPs (Fig. S8). Moreover, the difference between the two τ values of c-NGO/Au NPs and c-NGO/Au NPs-PEG, calculated for the green laser, further confirms the positive effect played by the PEG layer on the photothermal efficiency. On the other hand, under NIR laser light irradiation, c-NGO/Au NPs and c-NGO/Au NPs-PEG show similar τ values (Table S2), that account for the comparable temperature increase (ΔT of 15.20°C and 17.30°C, respectively) under the investigated experimental conditions, thus confirming that interactions between the plasmonic properties of the Au NPs and the c-NGO make c-NGO/Au NPs and c-NGO/Au NPs-PEG are able to convert NIR light into heat. However, the τ values reported in Table S2 clearly point out that the ΔT recorded under NIR laser is mainly due to light absorption phenomena, whilst the ΔT resulting from the irradiation with green laser is ascribable to thermoplasmonic phenomena.

### 3.11 *In vitro* investigation on the gastrointestinal cell viability upon exposure to the nanocomposites.

The effect of the c-NGO/Au NPs hybrid nanocomposites, synthesized with the 0.25:1 and 0.5:1 c-NGO:Au precursor w/w, both bare and HS-PEG functionalized (1:10 c-NGO:HS-PEG w/w), on viability of a gastric carcinoma cell line (N-87) and a normal epithelial colon cell line (HCEC-1CT), has been investigated by *in vitro* study to assess the suitability of the prepared highly densely coated nanocomposites in photothermal therapy applications. These cell lines have been selected, as PTT could play a relevant role in improving treatment effectiveness of cancers of the gastroenteric tract characterized by wide variability and complexity [60-62].

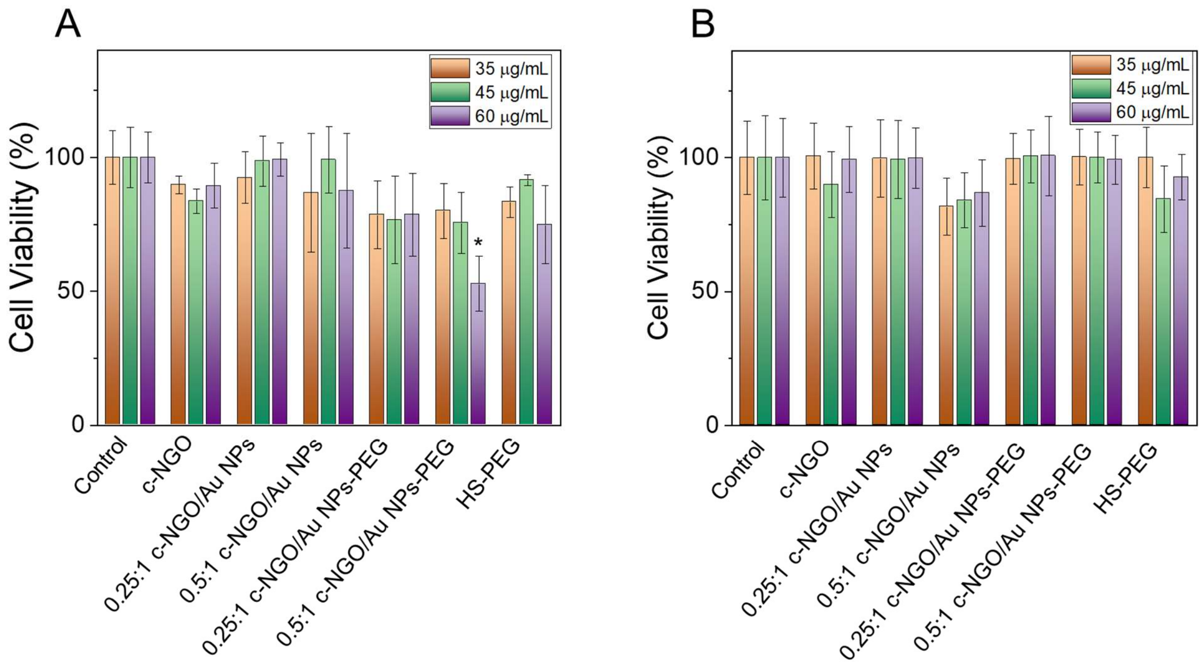

**Fig. 8.** Cell viability tests on HCEC-1CT (A) and N-87 (B) cell lines exposed to c-NGO, c-NGO/Au NPs (0.25:1 and 0.5:1 c-NGO:Au precursor w/w ratio), both bare and HS-PEG functionalized, for 72 h at 35, 45 and 60 µg mL$^{-1}$, respectively. Untreated cells have been used as control. *$p<0.05$.

The cells have been exposed to the nanocomposites at concentration ranging from 35 µg mL$^{-1}$ to 60 µg mL$^{-1}$ for 72 h. In the tested concentration range, no statistically significant effects on cell viability are observed upon treatment of the two cell lines with the hybrid nanocomposites, except for the highest tested concentration (60 µg mL$^{-1}$) of the c-NGO/Au NPs-PEG obtained with the 0.5:1 c-NGO:Au precursor w/w ratio, for which the cell viability of HCEC-1CT cells has been found reduced to 50% ($p<0.05$). No cytotoxicity in the normal and cancerous cells is also observed for the neat c-NGO and the free HS-PEG reference samples (Fig. 8A-B).

### 3.12 *In vitro* investigation of vimentin expression in gastrointestinal cell lines upon exposure to the nanocomposites.

*In vitro* investigation by immunofluorescence imaging has also been performed to detect possible changes in the vimentin expression, when HCEC-1CT and N-87 cells have been exposed to c-NGO, and c-NGO/Au NPs synthesized with 0.25:1 and 0.5:1 c-NGO:Au precursor w/w ratio, both bare and HS-PEG functionalized, for 72 h.

Confocal microscopy images of untreated and treated cells (Fig. 9A-B) and the corresponding immunofluorescence intensity index of vimentin (Fig. 9C-D) prove that a statistically significant upregulation of vimentin expression occurs upon exposure of both cell lines, for 72 h, to all tested c-NGO based nanocomposites, including also bare c-NGO and HS-PEG, with respect to control cells (Fig. 9).

Several studies have demonstrated that vimentin, a major constituent of the intermediate filament family of proteins, not only plays a decisive role in maintaining cellular integrity, but also becomes relevant in the response of cells exposed to a challenging event, such as heat or osmotic shock, treatment with inorganic compounds, or during wound healing, by increasing cellular mobility, and ensuring cell resistance to apoptosis against stress [63-66]. Recently, Patteson et al. have observed that the upregulation of vimentin occurs when cells prevent nuclei and mitochondria rupture, as well as genome disruption [67] with a temporary translocation into the nuclei [68]. Although the cell treatment with all tested hybrid nanocomposites, except for the sample c-NGO/Au NPs-PEG obtained with 0.5:1 c-NGO:Au NPs at 60 mg $mL^{-1}$, do not affect cell viability, a significant vimentin overexpression level, a stress response protein, is observed for all formulations, at all investigated concentrations (Fig. 9). Therefore, obtained data indicate that, although some stressful conditions arise from cell exposure to hybrid nanocomposites, cells can compensate this stress preserving their viability, as suggested, and supported by upregulation of vimentin. Furthermore, the percentage of nuclear localization of vimentin has been calculated on the base of the total number of nuclei for both cell lines and reported in Supplementary Materials (Table S3 and S4), to prove the temporary translocation of vimentin into nuclei as response to cellular stress induced by exposure to the hybrid nanocomposites, resulting in an enhancement of the vimentin expression percentage in the nuclei of the treated cells with respect to the control cells.

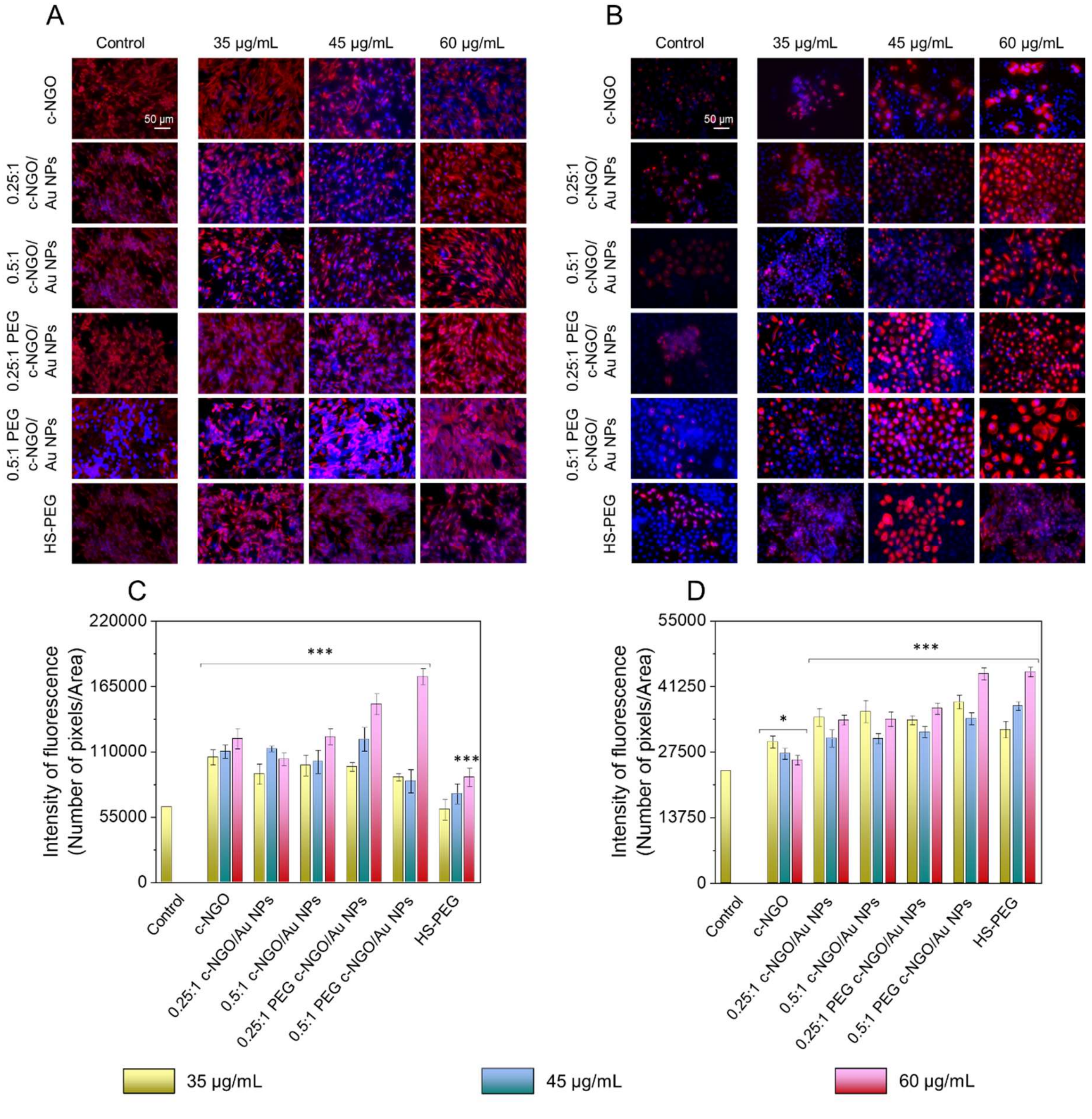

**Fig. 9.** Confocal images (A-B) and immunofluorescence analysis of vimentin (C-D) by HCEC-1CT (A-C) and N-87 (B-D) cells after treatment with c-NGO, c-NGO/Au NPs synthesized with 0.25:1 and 0.5:1 c-NGO:Au precursor w/w, as bare and functionalized with HS-PEG and HS-PEG for 72 h at 35, 45 and 60 µg $mL^{-1}$. Untreated cells were used as control. Overlay of blue stained nuclei and red labelled vimentin is shown for each cell line. Scale bar, 50 µm; magnification, 40×. * $p<0.05$; *** $p<0.001$

## 4. Conclusions

Water dispersible and biocompatible hybrid nanocomposites formed of carboxylated NGO sheets (c-NGO), highly densely coated with monodisperse, citrate-coated Au NPs, have been synthesized, by *in situ* reduction of $HAuCl_4 \times 3H_2O$ with citrate. The implementation of a preliminary step of NGO carboxylation by Williamson reaction, enhancing the -COOH groups density onto its basal plane, has made available a significant number of coordinating sites for assisting and directing NPs heteronucleation and growth onto NGO. The optimization of the synthetic parameters (i.e. c-NGO:Au precursor w/w ratio, Au precursor:citrate molar ratio, reaction temperature, Au precursor and citrate injection order in reaction mixture and c-NGO starting dispersion pH) along with the comprehensive characterization of the spectroscopic and morphological properties of resulting nanostructures, have enabled the control on the synthesis of nanocomposites, that have been achieved with a NPs coating density and monodispersion much higher than that reported for similar state-of-the-art materials. The systematic investigation of synthetic conditions has allowed also to get essential insights on the still not thoroughly elucidated synthesis mechanism.

The original theoretical model developed by conveniently combining DLS and TEM measurements has allowed to calculate the average number of Au NPs per NGO sheet, density value which is potentially useful for an accurate control of the nanocomposite functionalities. For the nanocomposite synthesized with the 160:1 citrate:Au precursor molar ratio and 0.25:1 c-NGO:Au precursor w/w ratio, at 100°C and 60 min reaction time, it has been found of 97.7 Au NPs per sheet.

Photothermal experiments, performed by irradiating the c-NGO/Au NPs-PEG hybrid nanocomposite at 532 nm and 808 nm, have shown a $\Delta T$ respectively of 20.00°C and 17.30°C, higher than that found for bare c-NGO.

The cytotoxicity and vimentin tests carried out on normal HCEC-1CT and gastric carcinoma N-87 cell lines, after exposure to the nanocomposites, before and after functionalization with PEG-SH, at concentrations ranging between 35-60 $\mu g\ mL^{-1}$, have demonstrated the overall retention of cell viability, along with a positive response to cell stress by vimentin expression increase.

Remarkably, the c-NGO/Au NPs and c-NGO/Au NPs PEG have exhibited light-to-heat conversion ability at a concentration value suitable to preserve the viability for both gastric carcinoma cells (N-87) and normal epithelial colon cells (HCEC-1CT).

Moreover, for the c-NGO/Au NPs and c-NGO/Au NPs PEG a temperature increase appropriate for PTT applications has been demonstrated. Indeed, about 2 min irradiation time is suitable for PPT-based treatment plans requiring minimal off-target effects.

Accordingly, the reported high photothermal activity and the demonstrated evidence of lack of cytotoxicity open the venue to applications of the nanocomposites in photothermal tumour ablation, also addressing, by means of suitably functionalized PEG, selective targeting to specific receptor sites of cancer cell to perform targeted therapy.

**Supplementary Material**. TEM micrographs, size distribution and UV-Vis-NIR absorption spectra of c-NGO/Au NPs achieved at reaction time of 60 min at 30°C, 70°C and 100°C. TEM micrographs of c-NGO/Au NPs achieved with 2:1 c-NGO:Au precursor w/w, 160:1 citrate:Au precursor molar ratio, at 100°C and reaction time of 10 min (A), 30 min (B) and 60 min (C). TEM micrographs of c-NGO/Au NPs achieved with 2:1 c-NGO:Au precursor w/w at 160:1 citrate:Au precursor molar ratio at 100°C injecting Au precursor in reaction flask filled with c-NGO and citrate, at reaction time of 10 min, 30 min and 60 min. Raman spectra of c-NGO and c-NGO/Au NPs. DLS traces and UV-Vis-NIR absorption spectra of c-NGO/Au NPs-PEG synthesized with 0.5:1 and 0.25:1 c-NGO:Au precursor w/w and with 1:1, 1:5 and 1:10 c-NGO:HS-PEG w/w. ATR-FTIR spectra of sodium citrate, c-NGO, HS-PEG and of c-NGO/Au NPs synthesized with 0.25:1 c-NGO: Au precursor w/w, as bare and functionalized with HS-PEG with 1:10 c-NGO:HS-PEG w/w. Absorption spectra of c-NGO, c-NGO/Au NPs and c-NGO/Au NPs-PEG at concentration of 45 μg mL$^{-1}$. Time-temperature dependence of c-NGO under pump beam irradiation at 532 nm (I=21 W· cm$^{-2}$) (A) and 808 nm (I=29 W· cm$^{-2}$) (B) at concentration of 45 μg mL$^{-1}$ in water.

## CRediT authorship contribution statement

Fabio Vischio: data curation, investigation, conceptualization, methodology, software, writing-reviewing and editing

Livianna Carrieri: data curation, investigation and conceptualization

Giuseppe Valerio Bianco: data curation, investigation and conceptualization, writing-reviewing and editing

Francesca Petronella: data curation, investigation and conceptualization, writing-reviewing and editing

Nicoletta Depalo: conceptualization and writing-reviewing

Elisabetta Fanizza: data curation, conceptualization, and writing-reviewing

Maria Principia Scavo: data curation, investigation, conceptualization, writing-reviewing and editing

Luciano De Sio: data curation, investigation and conceptualization writing-reviewing and editing

Antonella Calogero: funding acquisition

Marinella Striccoli: writing- reviewing and funding acquisition

Angela Agostiano: funding acquisition

Gianluigi Giannelli: funding acquisition

Maria Lucia Curri: conceptualization, writing-reviewing, editing and funding acquisition

Chiara Ingrosso: data curation, investigation, conceptualization, methodology, software, writing-reviewing and editing, funding acquisition and project administration

## Declarations of competing interest

The authors declare no conflict of interest including competing financial interests or personal relationships that could have appeared to influence the work reported in this paper.

## Acknowledgments

The work has been supported by Italian PON TITAN-Tumor Immunotherapy by Nanotechnology (ARS01_00906), University of Bari Horizon Europe Seeds Project BIOMAD, the Bilateral CNR-RFBR Project (2021-2023), bilateral CNR-MHESR TOOL project (2021-2022), PRIN 2017 "NiFTy" (prot. 2017MYBTXC), Italian TRANSISTOR project funded by INAIL (Bando BRIC 2019 ID:33), POR FESR LAZIO 2014-2020 - Project T0002E0001 "Photo-thermal cancer therapy based on radio-labelled gold nanoparticles-NANO-TAFT" (2020-2022) Grant N° 28166.

## References

[1] Y. Zhu, S. Murali, W. Cai, X. Li, J.W. Suk, J.R. Potts, R.S. Ruoff, Graphene and Graphene Oxide: Synthesis, Properties, and Applications, Adv. Mater., 22 (2010) 3906-3924. https://doi.org/10.1002/adma.201001068.

[2] G. Gonçalves, M. Vila, M.-T. Portolés, M. Vallet-Regi, J. Gracio, P.A.A.P. Marques, Nano-Graphene Oxide: A Potential Multifunctional Platform for Cancer Therapy, Adv. Healthcare Mater., 2 (2013) 1072-1090. https://doi.org/10.1002/adhm.201300023.

[3] Z. Li, H. Lei, A. Kan, H. Xie, W. Yu, Photothermal applications based on graphene and its derivatives: A state-of-the-art review, Energy, 216 (2021) 119262. https://doi.org/10.1016/j.energy.2020.119262.

[4] K. Yang, J. Wan, S. Zhang, B. Tian, Y. Zhang, Z. Liu, The influence of surface chemistry and size of nanoscale graphene oxide on photothermal therapy of cancer using ultra-low laser power, Biomaterials, 33 (2012) 2206-2214. https://doi.org/10.1016/j.biomaterials.2011.11.064.

[5] K.G. Thomas, S. Barazzouk, B.I. Ipe, S.T.S. Joseph, P.V. Kamat, Uniaxial Plasmon Coupling through Longitudinal Self-Assembly of Gold Nanorods, J. Phys. Chem. B, 108 (2004) 13066-13068. https://doi.org/10.1021/jp049167v.

[6] M. Schumacher, D. Jimenez de Aberasturi, J.-P. Merkl, L. Scarabelli, E. Lenzi, M. Henriksen-Lacey, L. M. Liz-Marzán, H. Weller, Robust Encapsulation of Biocompatible Gold Nanosphere Assemblies for Bioimaging via Surface Enhanced Raman Scattering, Advanced Optical Materials, 10 (2022) 2102635. https://doi.org/10.1002/adom.202102635.

[7] D.-K. Lim, A. Barhoumi, R.G. Wylie, G. Reznor, R.S. Langer, D.S. Kohane, Enhanced Photothermal Effect of Plasmonic Nanoparticles Coated with Reduced Graphene Oxide, Nano Lett., 13 (2013) 4075-4079. https://doi.org/10.1021/nl4014315.

[8] M. Cittadini, M. Bersani, F. Perrozzi, L. Ottaviano, W. Wlodarski, A. Martucci, Graphene oxide coupled with gold nanoparticles for localized surface plasmon resonance based gas sensor, Carbon, 69 (2014) 452-459. https://doi.org/10.1016/j.carbon.2013.12.048.

[9] G.V. Bianco, M.M. Giangregorio, M. Losurdo, A. Sacchetti, P. Capezzuto, G. Bruno, Demonstration of Improved Charge Transfer in Graphene/Au Nanorods Plasmonic Hybrids Stabilized by Benzyl Thiol Linkers, J. Nanomater, 2016 (2016) 2561326. https://doi.org/10.1155/2016/2561326.

[10] Y. Pan, S. Neuss, A. Leifert, M. Fischler, F. Wen, U. Simon, G. Schmid, W. Brandau, W. Jahnen-Dechent, Size-Dependent Cytotoxicity of Gold Nanoparticles, Small, 3 (2007) 1941-1949. https://doi.org/10.1002/smll.200700378.

[11] Q. Zhao, Y. Yang, H. Wang, W. Lei, Y. Liu, S. Wang, Gold nanoparticles modified hollow carbon system for dual-responsive release and chemo-photothermal synergistic therapy of tumor. J. Colloid Interface Sci, 554 (2019) 239-249. https://doi.org/10.1016/j.jcis.2019.07.005

[12] C. Wang, X. Wang, T. Lu, F. Liu, B. Guo, N. Wen, Y. Du, H. Lin, J. Tang, L. Zhang, Multi-functionalized graphene oxide complex as a plasmid delivery system for targeting hepatocellular carcinoma therapy, RSC Adv., 6 (2016) 22461-22468. https://doi.org/10.1039/C5RA21475K.

[13] Z. Wang, X. Sun, T. Huang, J. Song, Y. Wang, A Sandwich Nanostructure of Gold Nanoparticle Coated Reduced Graphene Oxide for Photoacoustic Imaging-Guided Photothermal Therapy in the Second NIR Window, Front. Bioeng. Biotechnol., 8 (2020). https://doi.org/10.3389/fbioe.2020.00655.

[14] Z. Zhang, H. Chen, C. Xing, M. Guo, F. Xu, X. Wang, H.J. Gruber, B. Zhang, J. Tang, Sodium citrate: A universal reducing agent for reduction / decoration of graphene oxide with au nanoparticles, Nano Res., 4 (2011) 599-611. https://doi.org/10.1007/s12274-011-0116-y.

[15] K. Patel, B. Bharatiya, T. Mukherjee, T. Soni, A. Shukla, B.N. Suhagia, Role of stabilizing agents in the formation of stable silver nanoparticles in aqueous solution: Characterization and stability study, J. Dispers. Sci. Technol., 38 (2017) 626-631. https://doi.org/10.1080/01932691.2016.1185374.

[16] F. Tarazona-Vasquez, P.B. Balbuena, Complexation of the Lowest Generation Poly(amidoamine)-$NH_2$ Dendrimers with Metal Ions, Metal Atoms, and Cu(II) Hydrates: An ab Initio Study, J. Phys. Chem. B, 108 (2004) 15992-16001. https://doi.org/10.1021/jp049324q.

[17] A.S.D.S. Indrasekara, R.C. Wadams, L. Fabris, Ligand Exchange on Gold Nanorods: Going Back to the Future, Part. Part. Syst. Charact., 31 (2014) 819-838. https://doi.org/10.1002/ppsc.201400006.

[18] G. Goncalves, P.A.A.P. Marques, C.M. Granadeiro, H.I.S. Nogueira, M.K. Singh, J. Grácio, Surface Modification of Graphene Nanosheets with Gold Nanoparticles: The Role of Oxygen Moieties at Graphene Surface on Gold Nucleation and Growth, Chem. Mater., 21 (2009) 4796-4802. https://doi.org/10.1021/cm901052s.

[19] P. Zhang, Y. Huang, X. Lu, S. Zhang, J. Li, G. Wei, Z. Su, One-Step Synthesis of Large-Scale Graphene Film Doped with Gold Nanoparticles at Liquid–Air Interface for Electrochemistry and Raman Detection Applications, Langmuir, 30 (2014) 8980-8989. https://doi.org/10.1021/la5024086.

[20] G.T. Hermanson, Introduction to Bioconjugation, in: G.T. Hermanson (Eds), Bioconjugate Techniques (Third Edition), Ed. Academic Press, Boston, 2013, pp. 1-125.

[21] M. Lotya, A. Rakovich, J. F. Donegan, J. N. Coleman, Measuring the lateral size of liquid-exfoliated nanosheets with dynamic light scattering, Nanotechnology, 24 (2013) 265703. https://doi.org/10.1088/0957-4484/24/26/265703.

[22] P. Szustakiewicz, N. Kołsut, A. Leniart, W. Lewandowski, Universal Method for Producing Reduced Graphene Oxide/Gold Nanoparticles Composites with Controlled Density of Grafting and Long-Term Stability, Nanomaterials, 9 (2019) 602. https://doi.org/10.3390/nano9040602.

[23] S. Feng, J. Lu, K. Wang, D. Di, Z. Shi, Q. Zhao, S. Wang, Advances in smart mesoporous carbon nanoplatforms for photothermal–enhanced synergistic cancer therapy. Chem. Eng. J., 435 (2022) 134886. https://doi.org/10.1016/j.cej.2022.134886.

[24] C. Chen, W. Kong, H.-M. Duan, J. Zhang, Theoretical simulation of reduction mechanism of graphene oxide in sodium hydroxide solution, Phys. Chem. Chem. Phys., 16 (2014) 12858-12864. https://doi.org/10.1039/C4CP01031K.

[25] M.P. Scavo, N. Depalo, F. Rizzi, C. Ingrosso, E. Fanizza, A. Chieti, C. Messa, N. Denora, V. Laquintana, M. Striccoli, M.L. Curri, G. Giannelli, FZD10 Carried by Exosomes Sustains Cancer Cell Proliferation, Cells, 8 (2019) 777. https://doi.org/10.3390/cells8080777.

[26] N. Depalo, E. Fanizza, F. Vischio, N. Denora, V. Laquintana, A. Cutrignelli, M. Striccoli, G. Giannelli, A. Agostiano, M.L. Curri, M.P. Scavo, Imaging modification of colon carcinoma cells exposed to lipid based nanovectors for drug delivery: a scanning electron microscopy investigation, RSC Adv., 9 (2019) 21810-21825. https://doi.org/10.1039/C9RA02381J.

[27] S. Lee, D.K. Lee, What is the proper way to apply the multiple comparison test?, Korean J. Anesthesiol., 71 (2018) 353-360. https://doi.org/10.4097/kja.d.18.00242.

[28] M.P. Scavo, F. Rizzi, N. Depalo, E. Fanizza, C. Ingrosso, M.L. Curri, G. Giannelli, A Possible Role of FZD10 Delivering Exosomes Derived from Colon Cancers Cell Lines in Inducing Activation of Epithelial–Mesenchymal Transition in Normal Colon Epithelial Cell Line, Int. J. Mol. Sci., 21 (2020) 6705. https://doi.org/10.3390/ijms21186705.

[29] A.C. Ferrari, Raman spectroscopy of graphene and graphite: Disorder, electron–phonon coupling, doping and nonadiabatic effects, Solid State Commun., 143 (2007) 47-57. https://doi.org/10.1016/j.ssc.2007.03.052.

[30] L.G. Cançado, A. Jorio, E.H.M. Ferreira, F. Stavale, C.A. Achete, R.B. Capaz, M.V.O. Moutinho, A. Lombardo, T.S. Kulmala, A.C. Ferrari, Quantifying Defects in Graphene via Raman Spectroscopy at Different Excitation Energies, Nano Lett., 11 (2011) 3190-3196. https://doi.org/10.1021/nl201432g.

[31] J. Amaro-Gahete, A. Benítez, R. Otero, D. Esquivel, C. Jiménez-Sanchidrián, J. Morales, Á. Caballero, F.J. Romero-Salguero, A Comparative Study of Particle Size Distribution of Graphene Nanosheets Synthesized by an Ultrasound-Assisted Method, Nanomaterials (Basel), 9 (2019) 152. https://doi.org/10.3390/nano9020152.

[32] Y. Park, J.Y. Koo, S. Kim, H.C. Choi, Spontaneous Formation of Gold Nanoparticles on Graphene by Galvanic Reaction through Graphene, ACS Omega, 4 (2019) 18423-18427. https://doi.org/10.1021/acsomega.9b02691.

[33] A. Van Hoonacker, P. Englebienne, Revisiting Silver Nanoparticle Chemical Synthesis and Stability by Optical Spectroscopy, Curr. Nanosci., 2 (2006) 359-371. https://dx.doi.org/10.2174/157341306778699310.

[34] H. Zhang, D. Hines, D.L. Akins, Synthesis of a nanocomposite composed of reduced graphene oxide and gold nanoparticles, Dalton Trans., 43 (2014) 2670-2675. https://doi.org/10.1039/C3DT52573B.

[35] A. Usher, D.C. McPhail, J. Brugger, A spectrophotometric study of aqueous Au(III) halide–hydroxide complexes at 25–80°C, Geochim. Cosmochim. Acta, 73 (2009) 3359-3380. https://doi.org/10.1016/j.gca.2009.01.036.

[36] I. Ojea-Jiménez, J.M. Campanera, Molecular Modeling of the Reduction Mechanism in the Citrate-Mediated Synthesis of Gold Nanoparticles, J. Phys. Chem. C, 116 (2012) 23682-23691. https://doi.org/10.1021/jp305830p.

[37] I. Ojea-Jiménez, F.M. Romero, N.G. Bastús, V. Puntes, Small Gold Nanoparticles Synthesized with Sodium Citrate and Heavy Water: Insights into the Reaction Mechanism, J. Phys. Chem. C, 114 (2010) 1800-1804. https://doi.org/10.1021/jp9091305.

[38] M. Tran, R. DePenning, M. Turner, S. Padalkar, Effect of citrate ratio and temperature on gold nanoparticle size and morphology, Mater. Res. Express, 3 (2016) 105027. https://doi.org/10.1088/2053-1591/3/10/105027.

[39] M. Wuithschick, A. Birnbaum, S. Witte, M. Sztucki, U. Vainio, N. Pinna, K. Rademann, F. Emmerling, R. Kraehnert, J. Polte, Turkevich in New Robes: Key Questions Answered for the

Most Common Gold Nanoparticle Synthesis, ACS Nano, 9 (2015) 7052-7071. https://doi.org/10.1021/acsnano.5b01579.

[40] F. Bettazzi, C. Ingrosso, P.S. Sfragano, V. Pifferi, L. Falciola, M.L. Curri, I. Palchetti, Gold nanoparticles modified graphene platforms for highly sensitive electrochemical detection of vitamin C in infant food and formulae, Food Chem., 344 (2021) 128692. https://doi.org/10.1016/j.foodchem.2020.128692.

[41] N.G. Bastús, J. Comenge, V. Puntes, Kinetically Controlled Seeded Growth Synthesis of Citrate-Stabilized Gold Nanoparticles of up to 200 nm: Size Focusing versus Ostwald Ripening, Langmuir, 27 (2011) 11098-11105. https://doi.org/10.1021/la201938u.

[42] C. Ingrosso, M. Corricelli, A. Disha, E. Fanizza, G.V. Bianco, N. Depalo, A. Panniello, A. Agostiano, M. Striccoli, M.L. Curri, Solvent dispersible nanocomposite based on Reduced Graphene Oxide and in-situ decorated gold nanoparticles, Carbon, 152 (2019) 777-787. https://doi.org/10.1016/j.carbon.2019.06.070.

[43] B. Derjaguin, L. Landau, Theory of the stability of strongly charged lyophobic sols and of the adhesion of strongly charged particles in solutions of electrolytes, Prog. Surf. Sci., 43 (1993) 30-59. https://doi.org/10.1016/0079-6816(93)90013-L.

[44] E.J.W. Verwey, Theory of the Stability of Lyophobic Colloids, J. Phys. Colloid Chem., 51 (1947) 631-636. https://doi.org/10.1021/j150453a001.

[45] S. Link, M.A. El-Sayed, Size and Temperature Dependence of the Plasmon Absorption of Colloidal Gold Nanoparticles, J. Phys. Chem. B, 103 (1999) 4212-4217. https://doi.org/10.1021/jp984796o.

[46] S. Karimi, A. Moshaii, S. Abbasian, M. Nikkhah, Surface Plasmon Resonance in Small Gold Nanoparticles: Introducing a Size-Dependent Plasma Frequency for Nanoparticles in Quantum Regime, Plasmonics, 14 (2019) 851-860. https://doi.org/10.1007/s11468-018-0866-4.

[47] L.H. Dubois, R.G. Nuzzo, Synthesis, Structure, and Properties of Model Organic Surfaces, Annu. Rev. Phys. Chem., 43 (1992) 437-463. https://doi.org/10.1146/annurev.pc.43.100192.002253.

[48] Y. Hu, C.-b. Sun, J. Kou, Exfoliation of poly(ethylene glycol)-intercalated graphite oxide composite in water without sonication, Int. J. Miner. Metall. Mater., 27 (2020) 840-845. https://doi.org/10.1007/s12613-019-1932-4.

[49] V. Lagesson, L. Lagesson-Andrasko, J. Andrasko, F. Baco, Identification of compounds and specific functional groups in the wavelength region 168–330 nm using gas chromatography with UV detection, J. Chromatogr. A, 867 (2000) 187-206. https://doi.org/10.1016/S0021-9673(99)01123-1.

[50] N.S. Vrandečić, M. Erceg, M. Jakić, I. Klarić, Kinetic analysis of thermal degradation of poly(ethylene glycol) and poly(ethylene oxide)s of different molecular weight, Thermochim. Acta, 498 (2010) 71-80. https://doi.org/10.1016/j.tca.2009.10.005.

[51] https://www.acsmaterial.com/single-layer-graphene-oxide-h-method.html.

[52] A.O. Govorov, H.H. Richardson, Generating heat with metal nanoparticles, Nano Today, 2 (2007) 30-38. https://doi.org/10.1016/S1748-0132(07)70017-8

[53] A. Guglielmelli, P. Rosa, M. Contardi, M. Prato, G. Mangino, S. Miglietta, V. Petrozza, R. Pani, A. Calogero, A. Athanassiou, G. Perotto, L. De Sio, Biomimetic keratin gold nanoparticle-mediated in vitro photothermal therapy on glioblastoma multiforme, Nanomedicine, 16 (2021) 121-138. https://doi.org/10.2217/nnm-2020-0349.

[54] L. De Sio, Active Plasmonic Nanomaterials, first ed., Jenny Stanford Publishing, New York 2015

[55] W. Lei, C. Sun, T. Jiang, Y. Gao, Y. Yang, Q. Zhao, S. Wang, Polydopamine-coated mesoporous silica nanoparticles for multi-responsive drug delivery and combined chemo-photothermal therapy. Mater. Sci. Eng. C, 105 (2019) 110103. https://doi.org/10.1016/j.msec.2019.110103

[56] Q. Chen, Y. Ren, H. Qi, L. Ruan, Influence of PEG coating on optical and thermal response of gold nanospheres and nanorods, J. Quant. Spectrosc. Radiat. Transf., 212 (2018) 1-9. https://doi.org/10.1016/j.jqsrt.2018.03.012.

[57] B. De Angelis, N. Depalo, F. Petronella, C. Quintarelli, M.L. Curri, R. Pani, A. Calogero, F. Locatelli, L. De Sio, Stimuli-responsive nanoparticle-assisted immunotherapy: a new weapon against solid tumours, J. Mater. Chem. B, 8 (2020) 1823-1840. https://doi.org/10.1039/C9TB02246E.

[58] K. Wang, J. Lu, J. Li, Y. Gao, Y. Mao, Q. Zhao, S. Wang, Current trends in smart mesoporous silica-based nanovehicles for photoactivated cancer therapy. J. Control. Release, 339 (2021) 445-472. https://doi.org/10.1016/j.jconrel.2021.10.005.

[59] D. K. Roper, W. Ahn, M. Hoepfner, Microscale Heat Transfer Transduced by Surface Plasmon Resonant Gold Nanoparticles. J. Phys. Chem. C, 111 (2007) 3636-3641. https://doi.org/10.1021/jp064341w.

[60] J. Zhang, T. Zhao, F. Han, Y. Hu, Y. Li, Photothermal and gene therapy combined with immunotherapy to gastric cancer by the gold nanoshell-based system, J. Nanobiotechnology, 17 (2019) 80. https://doi.org/10.1186/s12951-019-0515-x.

[61] M.I. Khot, H. Andrew, H.S. Svavarsdottir, G. Armstrong, A.J. Quyn, D.G. Jayne, A Review on the Scope of Photothermal Therapy-Based Nanomedicines in Preclinical Models of Colorectal Cancer, Clin. Colorectal Cancer, 18 (2019) e200-e209. https://doi.org/10.1016/j.clcc.2019.02.001.

[62] S.-J. Yang, H.-T. Huang, C.-H. Huang, J.-A. Pai, C.-H. Wang, M.-J. Shieh, The synergistic effect of chemo-photothermal therapies in SN-38-loaded gold-nanoshell-based colorectal cancer treatment, Nanomedicine, 17 (2022) 23-40. https://doi.org/10.2217/nnm-2021-0187.

[63] B.S. Buchmaier, A. Bibi, G.A. Müller, G.H. Dihazi, M. Eltoweissy, J. Kruegel, H. Dihazi, Renal Cells Express Different Forms of Vimentin: The Independent Expression Alteration of these Forms is Important in Cell Resistance to Osmotic Stress and Apoptosis, PLOS ONE, 8 (2013) e68301. https://doi.org/10.1371/journal.pone.0196935.

[64] F. Danielsson, M.K. Peterson, H. Caldeira Araújo, F. Lautenschläger, A.K.B. Gad, Vimentin Diversity in Health and Disease, Cells, 7 (2018) 147. https://doi.org/10.3390/cells7100147.

[65] C.S. Morrow, D.L. Moore, Vimentin's side gig: Regulating cellular proteostasis in mammalian systems, Cytoskeleton, 77 (2020) 515-523. https://doi.org/10.1002/cm.21645.

[66] S. Pattabiraman, G.K. Azad, T. Amen, S. Brielle, J.E. Park, S.K. Sze, E. Meshorer, D. Kaganovich, Vimentin protects differentiating stem cells from stress, Sci. Rep., 10 (2020) 19525. https://doi.org/10.1038/s41598-020-76076-4.

[67] A. E. Patteson, A. Vahabikashi, K. Pogoda, S.A. Adam, K. Mandal, M. Kittisopikul, S. Sivagurunathan, A. Goldman, R.D. Goldman, P.A. Janmey, Vimentin protects cells against nuclear rupture and DNA damage during migration, J. Cell Biol., 218 (2019) 4079-4092. https://doi.org/10.1083/jcb.201902046.

[68] S. Ceschi, M. Berselli, M. Cozzaglio, M. Giantin, S. Toppo, B. Spolaore, C. Sissi, Vimentin binds to G-quadruplex repeats found at telomeres and gene promoters, Nucleic Acids Res., 50 (2022) 1370-1381. https://doi.org/10.1093/nar/gkab1274.